7

Lasers in Atomic Collisions, Cold Plasma and Cold Atom Physics

R. Cabrera-Trujillo, J. Jiménez-Mier and A. M. Juárez
Universidad Nacional Autónoma de México
México

1. Introduction

In the more than 50 years since its conception, the laser and its variety of applications has covered most of the scientific and technological areas of science, from fundamental physics to biophysics and medicine. Probably, the scientific area that has benefited the most is the same area from where the laser originally came: Atomic, Molecular, and Optical (AMO) Physics. The purpose of this chapter is to present, through a selection of examples, how the applications of the laser in atomic collisions, cold plasmas and cold atom physics is still opening new areas of research. The examples chosen are a sample of what is the current research at the Instituto de Ciencias Nucleares (Nuclear Science Institute) and the Instituto de Ciencias Físicas (Physics Science Institute) at the Universidad Nacional Autónoma de México. We hope that, in choosing these examples, the reader will have the opportunity to get a wide view of three main areas of research in applications of lasers to AMO physics.
The chapter is separated in three sections. Section 2 deals with applications of numerical calculations related to laser assisted collisions, in particular the chapter deals with Finite Difference methods to the calculation of charge transfer cross sections. It shows the bits and pieces of how this numerical technique can be implemented. Section 3 shows an example of a calculation for experimental work with cold atoms. It discusses the technique of stimulated Raman adiabatic passage to produce highly excited Rydberg states. Finally, Sec. 4 shows the reader applications of the Optogalvanic Effect, and in particular to the new emergence of applications that are coming about due to the availability of solid state sources in the UV, and mid infrared. The applications of this technique go from simple basic physics research, to National Security, Biophysics and Medical applications.

2. Laser assisted charge transfer collisions

The study of ion-atom and ion-molecule interactions in the presence of an intense laser is a new and exciting field in atomic physics. Laser intensities up to $I = 3.5 \times 10^{16}$ W/cm^2 that correspond to the atomic unit of electric field $E = 5.1 \times 10^9$ V/cm are so intense that compete with the Columbic interaction force in the control of the electron dynamics. As a result, atoms and molecules in the presence of intense laser fields exhibit new properties and behavior which can be studied by means of multiphotonic processes. Those properties generate new behaviors of matter in the presence of intense lasers, with applications that go

from the study of ultra-fast phenomena, the development of lasers of high frequency (XUV and X-rays), the investigation of plasma properties and condensed matter under extreme conditions of temperature and pressure, up to the control of atomic and molecular reactions in the presence of intense lasers.
When an asymmetric collision occurs between an ion and an atom in the presence of an intense laser, the collision cross-section for the charge transfer induced by the laser can be several orders of magnitude greater than when it occurs without the presence of the laser (Anis et al. (2006); Cabrera-Trujillo (2009); Copeland & Tang (1976)).
In the first theoretical works on charge transfer induced by laser in a collision, the attention focused in resonant effects where the frequency of the laser was tuned to a transition in the colliding system (Copeland & Tang (1976); Ferrante et al. (1981); Gudzenko & Yakovenko (1972); Pindzola et al. (2003)). These calculations were carried out for very small intensities, or by means of perturbative calculations or for systems that could be considered coupled by two states in the presence of a laser field (Errea et al. (1983)). More recent work Kirchner (2002; 2004; 2005) has focused on laser intensities above 10^{13} W/cm^2 by using the basis generator method (BGM) with a CW laser. The BGM is a nonperturbative approach that has been successful in the study of field-free ion-atom collisions.
The objective of this section is to show the reader how the technique of finite differences can be used in problems of atomic collisions assisted by an intense laser as well as in the calculation of the cross-section for the charge transfer.

2.1 The problem

As an example, let us consider the case of a α particle (He^{2+}) colliding with a hydrogen atom. For this, we will consider favorable conditions to the experiment, that is to say, a laser of Ti:Sapphire of wavelength around 780 nm commonly used in experimental laboratories with an intermediate intensity of 3.5×10^{12} W/cm^2. In atomic units this corresponds to an electric field of $E_0 = 0.01$ a.u. and frequency $\omega = 0.057$ a.u.. These values guarantee that the effects of ionization and excitation due to the laser can be neglected.
A complete calculation based on quantum mechanics for the charge transfer induced by a laser is a very difficult problem, even computationally. For sufficiently high collisions energies, semi-classical models that consider classic trajectories and quantum electrons can be used. In addition, the interaction with the laser can be represented by means of the dipole approach. Thus, the electronic wave function satisfies the Time-Dependent Schröedinger equation (in atomic units)

$$i\frac{\partial}{\partial t}\Psi(\mathbf{r},t) = \Big[T + V(t)\Big]\Psi(\mathbf{r},t)\,, \tag{1}$$

where

$$T = -\frac{1}{2}\nabla^2\,, \tag{2}$$

$$V(\mathbf{r},t) = -\frac{Z_T}{|\mathbf{r}|} - \frac{Z_P}{|\mathbf{r}-\mathbf{R}_P(t)|} - \mathbf{E}(t)\cdot\mathbf{d}\ . \tag{3}$$

are the kinetic energy operator and the interaction potential, respectively. In this expression, Z_T and Z_P are the charges of the target and projectile, $\mathbf{R}_P(t)$ is the trajectory of projectile and $\mathbf{d} = -\mathbf{r}$ is the dipole moment of the electron. In this case, we will use the approach of

rectilinear trajectories for the projectile along the z-axis, that is to say,

$$\mathbf{R}_P(t) = b\hat{\mathbf{x}} + vt\hat{\mathbf{z}}\,, \tag{4}$$

where $b > 0$ is the impact parameter, v is the speed of the projectile commensurate to the collision energy, and $\hat{\mathbf{x}}$ and $\hat{\mathbf{z}}$ are the unitary vectors throughout the $x-$ and $z-$axes, respectively. For the laser we consider a pulse that reaches its maximum value at $t = 0$ and that agrees with the point of maximum approach between the projectile and the target. Explicitly, we used a Gaussian laser pulse given by:

$$\mathbf{E}(t) = \mathbf{E}_0 e^{-(\frac{t}{\tau})^2}\cos(\omega t + \varphi)\,, \tag{5}$$

where $\mathbf{E}_0$ is the amplitude of the electric field, $\tau\sqrt{4\log 2}$ defines the Full Width Half Maximum of the pulse (FWHM), ω is the frequency of the laser, and φ are the phase of the laser at the point of maximum approach in the collision. From this, it is clear that the dynamics of the collision is governed by a differential equation of second order [Eq. (1)], which we required to solve as a function of time.

2.2 Physics on a numerical lattice

The physics of many time-dependent problems can be described by a systems of coupled partial differential equations (generally nonlinear), complemented by the initial and boundary conditions of the system. An example is the Schröedinger equation (in 1-D)

$$\Big\{-\frac{\hbar^2}{2\mu}\frac{\partial^2}{\partial x^2} + V(x)\Big\}\Psi(x,t) = i\hbar\frac{\partial}{\partial t}\Psi(x,t)\,, \tag{6}$$

or in the time-independent case

$$\Big\{-\frac{\hbar^2}{2\mu}\frac{\partial^2}{\partial x^2} + V(x)\Big\}\Psi(x) = E\Psi(x)\,. \tag{7}$$

Here μ is the mass of the particle under the effect of the potential $V(x)$. To solve this system of differential equations, we use the finite difference method. The concept of the finite difference approximation to systems that evolve in the time can be illustrated if we consider a problem in 1+1 dimensions (x,t). A numerical lattice is shown in the Fig. 1 which consists of a system of fixed positions x_k, that may or may not be spaced uniformly, and that are defined in the discreet time t^n.

2.2.1 Functions

If the value of a function $f(x,t)$ in the point (x,t) is associated to a point in the lattice, then

$$f(x,t) = f(x_k,t^n) \to f_k^n\,. \tag{8}$$

Note that we use subscripts to represent spatial dependence in the lattice point and superscript to denote temporal dependence.

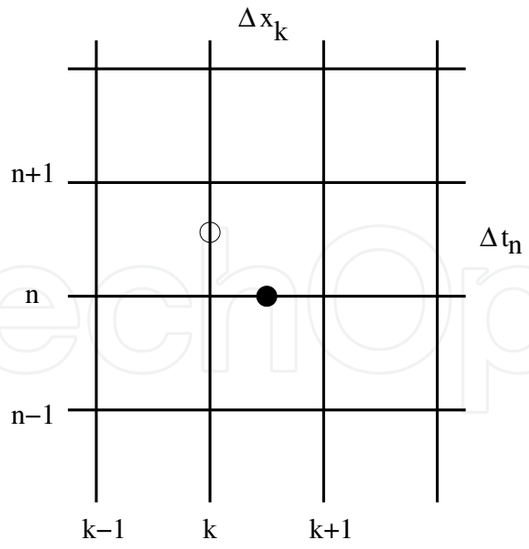

Fig. 1. Uniform numerical lattice in space-time with constant $\Delta x = \Delta x_k^n$ and $\Delta t = \Delta t_k^n$.

2.2.2 Partial derivatives

The finite difference approximation of the partial derivative of $f(x,t)$ can be constructed from the Taylor expansion around x_0. This gives

$$f(x_0 + \Delta x, t) = f(x_0) + \frac{\partial f}{\partial x}\Big|_{x_0} \Delta x + \frac{1}{2}\frac{\partial^2 f}{\partial x^2}\Big|_{x_0} \Delta x^2 + O(\Delta x^3) \tag{9}$$

and

$$f(x_0 - \Delta x, t) = f(x_0) - \frac{\partial f}{\partial x}\Big|_{x_0} \Delta x + \frac{1}{2}\frac{\partial^2 f}{\partial x^2}\Big|_{x_0} \Delta x^2 + O(\Delta x^3)\,. \tag{10}$$

From Eq. (9) to first order, we obtain what is known as a forward difference equation

$$\frac{\partial f}{\partial x}\Big|_{x_0} = \frac{f(x_0 + \Delta x) - f(x_0)}{\Delta x} + O(\Delta x^2)\,. \tag{11}$$

Similarly, from Eq. (10) we obtain what is know as a backward difference equation

$$\frac{\partial f}{\partial x}\Big|_{x_0} = \frac{f(x_0) - f(x_0 - \Delta x)}{\Delta x} + O(\Delta x^2)\,. \tag{12}$$

An approximation to second order for the second derivative is obtained by adding Eqs. (9) and (10):

$$\frac{\partial^2 f}{\partial x^2}\Big|_{x_0} = \frac{f(x_0 + \Delta x) - 2f(x_0) + f(x_0 - \Delta x)}{\Delta x^2} + O(\Delta x^3)\,. \tag{13}$$

Let us suppose that $f(x,t)$ correspond to a point in the spatial lattice: $x_0 \to x_k$, $x_0 + \Delta x \to x_{k+1}$, and $f(x,t) \to f_k^n$, then from Eq. (11)

$$\frac{\partial f}{\partial x}\Big|_{x_k} = \frac{f_{k+1} - f_k}{x_{k+1} - x_k} + O(\Delta x^2)\,, \tag{14}$$

which represent a forward approximation in space to $(\partial f/\partial x)_{x_k}$ in the k-th lattice point. In the same way, from Eq. (12) the backward approximation is

$$\frac{\partial f}{\partial x}\Big|_{x_k} = \frac{f_k - f_{k-1}}{x_k - x_{k-1}} + O(\Delta x^2)\,. \tag{15}$$

And for the second order partial derivative of $f(x,t)$ in the uniform spatial lattice point x_k one obtains:

$$\frac{\partial^2 f}{\partial x^2}\Big|_{x_k} = \frac{f_{k+1} - 2f_k + f_{k-1}}{(\Delta x)^2} + O(\Delta x^3)\,. \tag{16}$$

2.2.3 Integrals

If we are required to calculate an integral, for example, when normalizing the solution to the Schrödinger equation, we can use the Riemann definition for an integral, that is

$$\int f(x)dx = \sum_{k=1}^{N-1} f_k(x_{k+1} - x_k)\,, \tag{17}$$

that for a uniform lattice becomes

$$\int f(x)dx = \sum_{k=1}^{N-1} f_k \Delta x\,. \tag{18}$$

2.3 Time-independent case

In the particular case in which we are required to solve the Time-Independent Schrödinger equation the approximation to the differential equation in finite differences is obtained replacing Eq. (16) into Eq. (7). Therefore, for a uniform lattice with $x_{k+1} - x_k = \Delta x$

$$-\frac{\hbar^2}{2\mu}\left\{\frac{\Psi_{k+1} - 2\Psi_k + \Psi_{k-1}}{\Delta x^2}\right\} + V_k\Psi_k = E\Psi_k \tag{19}$$

where we have omitted the temporal dependency.

Since $k = \{1, ..., N\}$, where N is the number of points in the lattice, then Eq. (19) has a complete solution when we specify the initial and boundary conditions. In our case, $\Psi(x,t) \in \mathcal{L}^2$, that is, it is square integrable such that in the boundary $\{-\infty, \infty\}$ the function is zero. In our case, we do not have a lattice that covers an infinite extension of the space, so we adjust ourselves to a finite lattice where the initial and final points form the boundaries. From here, $\Psi_{k=0} = 0$ and $\Psi_{k=N+1} = 0$ such that

$$-\frac{\hbar^2}{2\mu\Delta x^2}\Big\{\Psi_2 - 2\Psi_1\Big\} + V_1\Psi_1 = E\Psi_1 \tag{20}$$

and

$$-\frac{\hbar^2}{2\mu\Delta x^2}\Big\{-2\Psi_N+\Psi_{N-1}\Big\}+V_N\Psi_N=E\Psi_N\,. \tag{21}$$

Equation (19) together with the boundary conditions (20) and (21) can be written in matrix form by making a vector array $\vec{\mathbf{\Psi}}=\{\Psi_k\}$. Thus

$$\mathbf{H}\vec{\mathbf{\Psi}}=E\vec{\mathbf{\Psi}} \tag{22}$$

where $\mathbf{H}$ has the matrix elements given by

$$\begin{aligned} H_{i,i}&=\frac{\hbar^2}{\mu\Delta x^2}+V_k\,,\\ H_{i,i+1}&=-\frac{\hbar^2}{2\mu\Delta x^2}\,,\\ H_{i,i-1}&=-\frac{\hbar^2}{2\mu\Delta x^2}\,, \end{aligned} \tag{23}$$

which is a Hermitian tridiagonal matrix of the form:

$$\mathbf{H}=\begin{pmatrix} H_{1,1} & H_{1,2} & 0 & 0 & \cdots & 0\\ H_{2,1} & H_{2,2} & H_{2,3} & 0 & \cdots & 0\\ 0 & H_{3,2} & H_{3,3} & H_{3,4} & \cdots & 0\\ \vdots & \vdots & \vdots & \ddots & \vdots & \vdots\\ 0 & \cdots & 0 & H_{N-1,N-2} & H_{N-1,N-1} & H_{N-1,N}\\ 0 & \cdots & 0 & 0 & H_{N,N-1} & H_{N,N} \end{pmatrix}. \tag{24}$$

Equation (22) thus represents an eigenvalue problem in matrix algebra with the advantage of being a tridiagonal matrix. The number of eigenvectors and eigenvalues depends on the number of points in the numerical lattice.

2.4 Time-dependent case

For the time-dependent case, we use Eq. (6) and applying the finite difference approximation we get

$$-\frac{\hbar^2}{2\mu}\left\{\frac{\Psi^n_{k+1}-2\Psi^n_k+\Psi^n_{k-1}}{\Delta x^2}\right\}+V_k\Psi^n_k=i\hbar\frac{\Psi^{n+1}_k-\Psi^n_k}{t^{n+1}-t^n}\,. \tag{25}$$

Thus, for a constant increment in time $\Delta t=t^{n+1}-t^n$ we have that the wave function at time $t=t^n+\Delta t$ is given by

$$-\frac{\hbar\Delta t}{i2\mu\Delta x^2}\Big\{\Psi^n_{k+1}-2\Psi^n_k+\Psi^n_{k-1}\Big\}-\frac{i\Delta t}{\hbar}V_k\Psi^n_k+\Psi^n_k=\Psi^{n+1}_k\,. \tag{26}$$

This equation is an example of a explicit method, since the solution at a later time is given in terms of the previous time. The last equation can be written as

$$\vec{\Psi}^{n+1} = \left\{1 - \frac{i\Delta t}{\hbar}\mathbf{H}\right\}\vec{\Psi}^{n}\,. \tag{27}$$

But from Eq. (6) we know that the time-dependent solution for the time-independent Hamiltonian $\hat{\mathbf{H}}$ is

$$\Psi(x,t) = e^{-i\frac{(t-t_0)}{\hbar}\hat{\mathbf{H}}}\Psi(x,t_0)\,, \tag{28}$$

thus we can use the previous equation together with the finite difference method to obtain a improved solution in time for the wave function.

2.4.1 Crank-Nicolson method

By using the split-operator technique, we can write Eq. (28) as

$$\Psi(x,t) = e^{-i\frac{\Delta t}{\hbar}\left\{\hat{\mathbf{T}}+V(x)\right\}}\Psi(x,t_0) \tag{29}$$

where $\Delta t = t - t_0$. Separating the operator for the kinetic energy

$$\Psi(x,t) \simeq e^{-i\frac{\Delta t}{2\hbar}\hat{\mathbf{T}}}e^{-i\frac{\Delta t}{2\hbar}\hat{\mathbf{T}}}e^{-i\frac{\Delta t}{\hbar}V(x)}\Psi(x,t_0)\,, \tag{30}$$

therefore

$$e^{i\frac{\Delta t}{2\hbar}\hat{\mathbf{T}}}\Psi(x,t) \simeq e^{-i\frac{\Delta t}{2\hbar}\hat{\mathbf{T}}}e^{-i\frac{\Delta t}{\hbar}V(x)}\Psi(x,t_0)\,. \tag{31}$$

Defining

$$f(x,t,t_0) = e^{-i\frac{\Delta t}{\hbar}V(x)}\Psi(x,t_0)\,, \tag{32}$$

we get, to first order in the exponential,

$$\left\{1 + i\frac{\Delta t}{2\hbar}\hat{\mathbf{T}}\right\}\Psi(x,t) = \left\{1 - i\frac{\Delta t}{2\hbar}\hat{\mathbf{T}}\right\}f(x,t,t_0)\,. \tag{33}$$

Since the kinetic energy operator is $\hat{\mathbf{T}} = -\frac{\hbar^2}{2\mu}\frac{\partial^2}{\partial x^2}$, then applying the finite difference method to the previous equation, we get

$$\left\{\Psi_k^{n+1} - i\frac{\hbar\Delta t}{4\mu\Delta x^2}\left(\Psi_{k+1}^{n+1} - 2\Psi_k^{n+1} + \Psi_{k-1}^{n+1}\right)\right\} = \left\{f_k + i\frac{\hbar\Delta t}{4\mu\Delta x^2}\left(f_{k+1} - 2f_k + f_{k-1}\right)\right\}\,, \tag{34}$$

or in matrix form

$$\mathbf{A}^{+}\vec{\Psi}^{n+1} = \mathbf{A}^{-}\vec{f}\,, \tag{35}$$

therefore

$$\vec{\Psi}^{n+1} = (\mathbf{A}^{+})^{-\mathbf{1}}\mathbf{A}^{-}\vec{f}\,. \tag{36}$$

This is the implicit Crank-Nicolson method, where in both sides of the equation the final time appears. The matrices $\mathbf{A}^{+}$ y $\mathbf{A}^{-}$ are tridiagonal matrices with elements given by

$$\begin{aligned} A_{i,i}^{\pm} &= 1 \pm 2\nu\,, \\ A_{i,i+1}^{\pm} &= \mp\nu\,, \\ A_{i,i-1}^{\pm} &= \mp\nu\,, \end{aligned} \tag{37}$$

where $\nu = \frac{i\hbar\Delta t}{4\mu\Delta x^2}$. That is

$$\mathbf{A}^{\pm} = \begin{pmatrix} 1 \pm 2\nu & \mp\nu & 0 & 0 & \cdots & 0 \\ \mp\nu & 1 \pm 2\nu & \mp\nu & 0 & \cdots & 0 \\ 0 & \mp\nu & 1 \pm 2\nu & \mp\nu & \cdots & 0 \\ \vdots & \vdots & \vdots & \ddots & \vdots & \vdots \\ 0 & \cdots & 0 & \mp\nu & 1 \pm 2\nu & \mp\nu \\ 0 & \cdots & 0 & 0 & \mp\nu & 1 \pm 2\nu \end{pmatrix}. \tag{38}$$

Thus, the temporal evolution of a system can be solved by means of linear algebra approaches, for example, the LU matrix decomposition (Press et al. (1992)).
The extension to a 2- or 3-D case is straightforward since the procedure can be nested in several loops, each one for a dimension.

2.5 Implementation

Although the finite difference method is straightforward, the calculations are computationally intensive and we must take care in obtaining stable and precise results. One of the problems that arises is when the charged projectile moves in the numerical lattice, since when the projectile passes over the $\mathbf{R}_P = \mathbf{r}$, i.e. a point on the lattice, there appears a singularity in the potential and the numerics will behave as if a collision with a wall. Inclusively, if the projectile passes close, there is a periodic oscillating effect when the projectile approaches each point of the lattice as it moves. In order to solve this problem, a damping or soft-core parameter can be introduced in the Coulomb potential. Nevertheless, one finds that this procedure overestimates the charge transfer. A simple solution to this problem consists of placing the trajectory of projectile in the center of the squares defined by the points of the lattice in the plane defined by the collision. One second approach is to fix the position of the He^{2+} ion to the origin to diminish fluctuations due to the large nuclear charge of the projectile. Thus, the hydrogen atom becomes the projectile in this reference system (Galilean transformation). This change only introduces a phase factor in the wave function. In this work we opted for the center of the lattice method.
The numerical lattice used in our implementation of finite differences covers the region $[-6 : 15]_x \times [-6 : 6]_y \times [-25 : 25]_z$ u.a. The size of this lattice was chosen in such a way that it balances the time of calculation and the precision of the physical results. The size of the lattice was chosen of $\Delta x = \Delta y = \Delta z = 0.2$ u.a., which gives a ground energy for the hydrogen atom of $E_H = -0.490$ u.a and of $E_{He^+} = -1.90$ u.a for the ground state of the Helium ion.
Our calculations cover the temporal range from $t_i = -200$ to $t_f = 200$ u.a which gives us sufficient time to separate clearly, the projectile and target at the end of the collision for a collision energy of 1 keV. The size of the temporary step was chosen as 0.06 u.a in such a way that it balances the time that the dynamics take and to preserve the precision of the calculations. It was chosen on the basis of several tests of energy conservation.

2.5.1 Charge transfer

We calculate the charge transfer probability by means of the integration of the electronic charge density over a box Ω_T, that encloses the projectile at the final time of the collision

t_f,

$$P = \int_{\Omega_T} |\Psi(\mathbf{r}, t_f)|^2 d^3\mathbf{r} \equiv \int_{z_T}^{z_{max}} \rho_z(z, t_f) dz \ , \tag{39}$$

where z_T defines the mid point distance between target and projectile and where the charge density $\rho_z(z,t)$ is given by

$$\rho_z(z,t) = \int_{x_{min}}^{x_{max}} \int_{y_{min}}^{y_{max}} |\Psi(x,y,z,t)|^2 \, dx \, dy \, .$$

Therefore it is required that the contributions of the target and the projectile to the wave function are clearly separated in the space, as is shown in the example of the Fig 2. Once the capture probability of electrons is obtained as a function of the impact parameter, we can calculate the cross-section for charge transfer. From conservation of the number of particles in the collision, we have that if I is the intensity of colliding particles per unit area, unit time (that is to say, the particle flux), then $I\, b\, db\, d\phi$ is the number of particles per unit time that interact with the target. This number must be equal to the number of scattered particles in collision per unit of solid angle, $I(d\sigma/d\Omega)d\Omega$, that is to say, the number of scattered particles is proportional to the number of colliding particles per unit of solid angle. Here, the constant of proportionality, $d\sigma/d\Omega$, is the scattering probability and has units of area, and therefore the name of cross-section of the collision. Therefore, since $d\Omega = \sin(\theta) d\theta d\phi$ then

$$\frac{d\sigma}{d\Omega} = \frac{b}{\sin(\theta)} \left| \frac{db}{d\theta} \right|$$

is the differential scattering cross section.

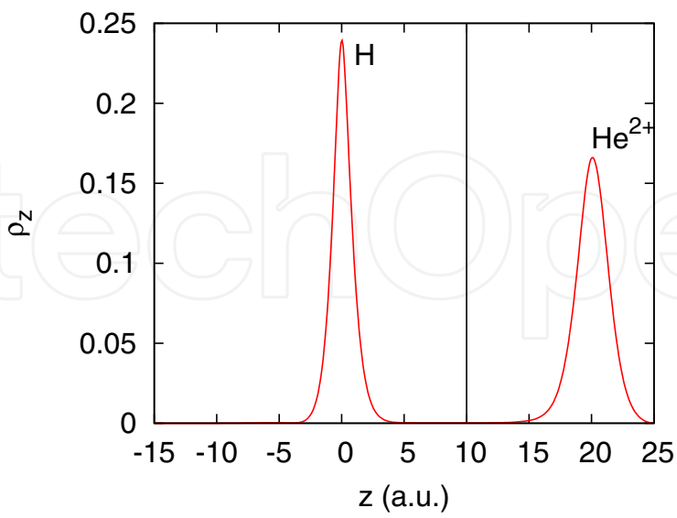

Fig. 2. Example of electronic density ρ_z for He^{++}+H at $b = 0.4$ u.a., $E_0 = 0$ (No field) and a collision energy of 1 keV/amu. The dotted line at $z = 10$ a.u. separates the boundary Ω_T for the projectile (see text).

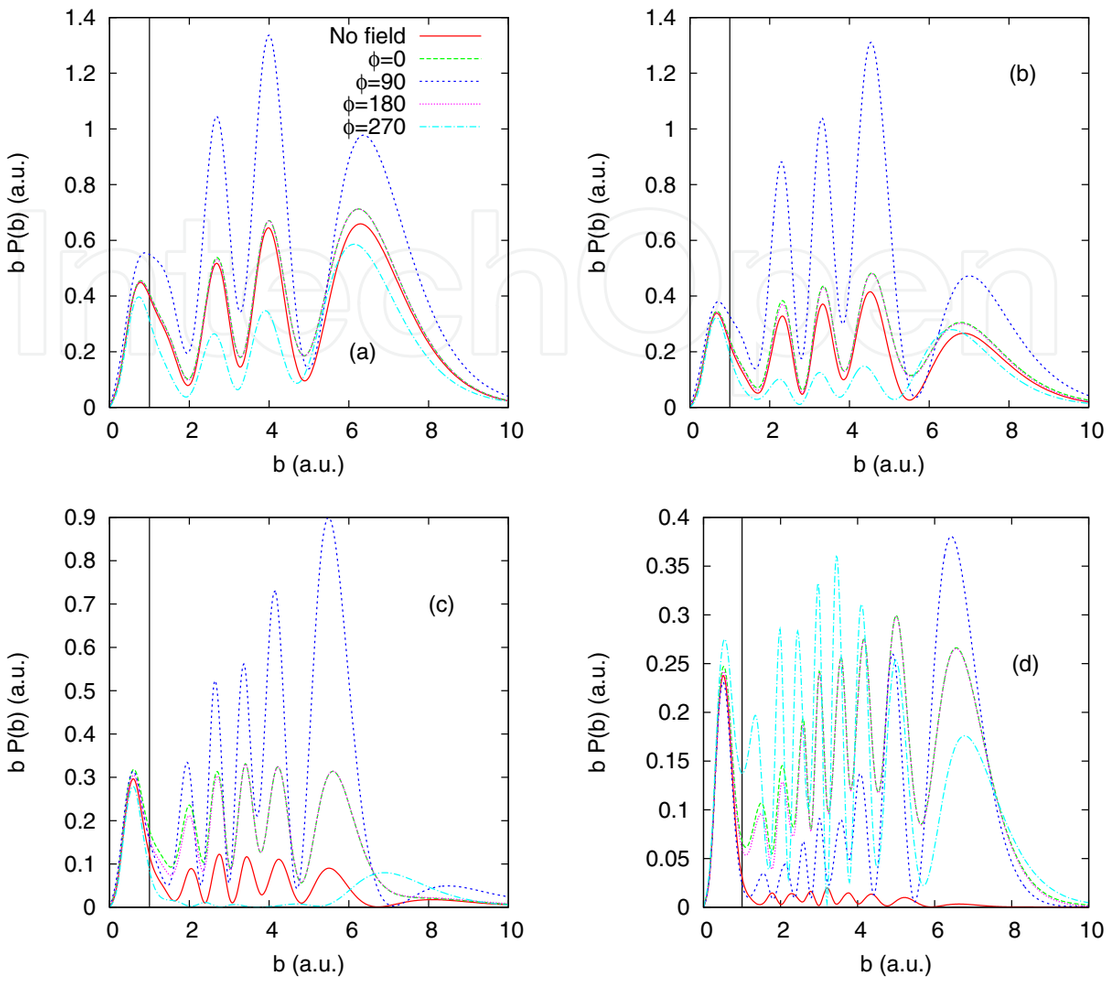

Fig. 3. Impact parameter weighted probability for charge transfer, $bP(b)$, as a function of the impact parameter for laser phase $\phi = 0$, 90, 180, and 270 deg. The results are shown for collision energies of a).- $E = 1.5$; b).- $E = 1.0$; c).- $E = 0.5$; and d).- $E = 0.25$ keV/amu. The results are for a laser field of intensity $I = 3.5 \times 10^{12}$ W/cm^2, wavelength $\lambda = 780$ nm, and FWHM of 6 fs with polarization parallel to the axis of the collision.

For the case of a processes with probability $P(b)$ for each impact parameter or scattering angle, the differential cross section is given by

$$\frac{d\sigma}{d\Omega} = \frac{b\,P(b)}{\sin(\theta)} \left| \frac{db}{d\theta} \right| .$$

Integrating over all the scattering angles we find the total scattering cross section is:

$$\sigma = 2\pi \int_0^\infty b\,P(b)\,db\,. \tag{40}$$

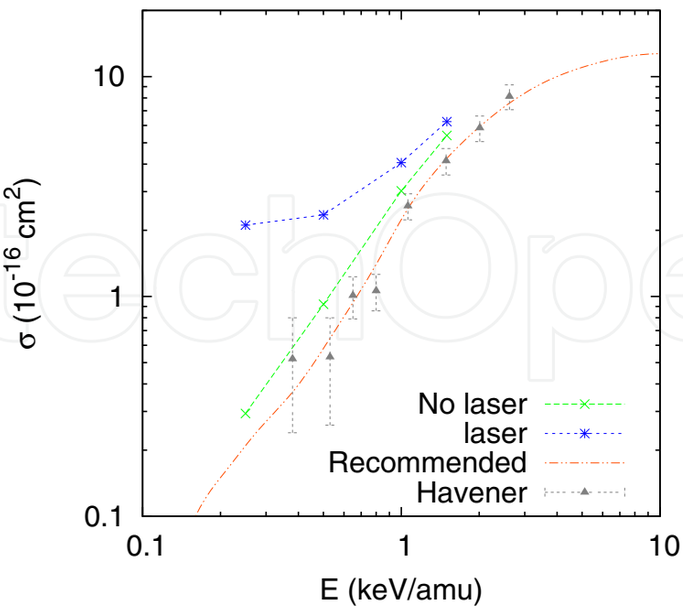

Fig. 4. Electron charge transfer cross section as a function of the projectile energy. The dashed line is the finite difference result without laser. The dotted line is the result with laser field averaged over the phase ϕ. The up-triangle symbols are the experimental data from from Havener (Havener et al. (2005)), as well as the dot-dashed line that corresponds to their recommended laser-free theoretical results, respectively.

2.6 Results

In Fig. 3, we show the results for the weighted electron capture probability as a function of the impact parameter for a laser carrier phase of 0, 90, 180, and 270 deg and electric field parallel to the axis of the collision and for collision energies of $E = 1.5$ keV/amu (Fig. 3a), $E = 1.0$ keV/amu (Fig. 3b), $E = 0.5$ keV/amu (Fig. 3c), and $E = 0.25$ keV/amu (Fig. 3d). In the same figure, we show the results without laser field (solid line). The effect of the laser field occurs for impact parameter larger than $b > 2.0$ a.u. in the so called radial region (Stolterfoht et al. (2007)). For impact parameters $b < 2.0$ the effect is small, in the so called rotational region. This two regions are shown by the vertical line in Fig. 3. In the high energy cases, the largest contribution comes from $\phi = 90$ deg, while the lower contribution is from $\phi = 270$ deg. At high energies, they average mostly to the case without laser field. For low collision energies, however, the electron capture can be up to one order of magnitude larger for the collision energies considered in this work. The total cross-section for the charge transfer induced by the field laser is shown in fig 4 for the case in that the electric field of the laser parallel to the axis of the collision and we compared with the results without field laser as a function of the collision energy. In the same figure, we compare our results to the experimental data without laser field of Havener (Havener et al. (2005)) as well as their recommended theoretical values. First we noticed a good agreement between the experimental results and our cross sections obtained by the finite difference approach for the case of no laser field. In the case of laser field we observe an increase in the cross-section for charge transfer by a factor of up to ~ 10 for low collision energies.

2.7 Conclusions

The presence of an intense laser field in the atom interaction produces a great variety of effects that allow us to the control processes such as generation of harmonics, above threshold ionization, Coulomb explosion, etc. The dynamics of these processes is governed by the time-dependent Schrödinger equation. In this section we have shown how the finite difference method can be used to obtain dynamic numerical solutions and thus to study the interaction process. In the case of atomic collisions in the presence of a laser we have found that for the case of He^{2+} colliding with atomic hydrogen the cross-section of electronic capture intensifies up to a factor of six in average, for a 10 fs Gaussian laser pulse and intensity of $3,5 \times 10^{12}$ W/cm^2 for energies of collision in the region of keV.

3. Laser pulses for the coherent manipulation of quantum states in cold atoms.

A controlled sequence of laser pulses can be used to manipulate quantum states of matter. In particular, the technique of stimulated Raman adiabatic passage (STIRAP) uses a counterintuitive pulse sequence to efficiently transfer population between two long lived states of a system (Carroll & Hioe (1988); Kuklinski et al. (1989); Oreg et al. (1985; 1984)). The basic STIRAP scheme involves three states, the initial state $|0\rangle$, the intermediate state $|1\rangle$ and the final state $|2\rangle$, excited by two laser pulses that partially overlap in time. Usually the intermediate state $|1\rangle$ is short lived, and it may decay into other states of the system. The goal is to transfer the entire population initially in state $|0\rangle$, to the target state $|2\rangle$. This is accomplished by applying a first (Stokes) pulse in near resonance with the energy difference between states $|1\rangle$ and $|2\rangle$ followed by a pump pulse in near resonance with the $|0\rangle$ to $|1\rangle$ transition. If this counterintuitive sequence of pulses is applied maintaining adiabatic evolution conditions, a trapped or dark state is produced and it evolves from the initial state $|0\rangle$ into the final state$|2\rangle$ without ever passing through the intermediate state.

There are several examples of both theoretical and experimental studies of three-level two-pulse STIRAP (Bergmann et al. (1998)). There are also detailed theoretical studies that extend the analysis of STIRAP processes to more than three levels (Malinovsky & Tannor (1997); Oreg et al. (1992); Smith (1992); Vitanov (1998); Vitanov et al. (1998)). Here a clear difference can be established between systems with an odd number of levels, for which a dark state can be immediately identified, and systems with even number of levels, that strictly never have such state (Smith (1992); Vitanov (1998)).

Cold atoms are the perfect laboratory to test coherent state manipulation using light. The cooling and trapping process allows one to produce a cloud of atoms in a specific quantum state (Metcalf & van der Straten (1999)). The translational temperature can range between a few mK to a few nK, and therefore Doppler effects in the interaction between the atoms and electromagnetic radiation are strongly reduced. At these temperatures the atoms move so slowly that in the interaction time they suffer no collisions. The first experiments to study STIRAP with cold atoms used the $5s \rightarrow 5p \rightarrow 5d$ ladder excitation in rubidium (Süptitz et al. (1997)). STIRAP to produce coherent excitation of cold atoms into Rydberg states has also been demonstrated in rubidium magneto-optical traps (Cubel et al. (2005); Deiglmayr et al. (2006)). Cold rubidium atoms have also been used to study in great detail the population dynamics in a STIRAP process (Gearba et al. (2007)). In all these examples the basic three-level and two-pulse STIRAP scheme was used.

Cold Rydberg atoms are at the core of very interesting proposals for quantum information processes with neutral atoms. A recent review was published by Saffman *et al.* (Saffman et al. (2010)). The central idea is to use long range interactions between Rydberg atoms to produce quantum gates. An important requirement posed by these quantum gate protocols is a precise coherent excitation and de-excitation of Rydberg states (Saffman et al. (2010)). The widely used scheme is to excite into a Rydberg state by two-photon excitation starting from the atomic ground state. For example, the excitation $5s \rightarrow 5p_{3/2} \rightarrow n\ell$ in rubidium requires a 780 nm photon for the first step and a wavelength of about 480 nm for the second step, in order to reach the Rydberg state. These were the excitations used to show efficient population transfer into Rydberg states using STIRAP (Cubel et al. (2005); Deiglmayr et al. (2006)). The transition matrix element for excitation into a Rydberg state nℓ is small and it decreases with increasing quantum number according to the power law $n^{-3/2}$ (Saffman et al. (2010)). Using the $5p_{3/2}$ level in rubidium for STIRAP production of Rydberg states therefore requires high laser powers and tight focusing into the cold atom cloud. Also, to extend the STIRAP efficiency to higher n's the laser power has to be scaled by n^3.

In this section we present a theoretical analysis of an alternative, four-level STIRAP scheme to transfer the population of the 5s atomic ground state into long-lived Rydberg states of cold rubidium atoms. It considers as intermediate states the $5p_{3/2}$ and 5d atomic levels and therefore has the advantage of requiring the use of lower power diode lasers to produce the STIRAP pulses (Thoumany et al. (2009)). Furthermore, because the 5d radial wave function extends further out, one expects the transition matrix elements connecting to the np or nf Rydberg states to be larger than the corresponding transition matrix elements between the $5p_{3/2}$ and the ns or nd states. We also show the results of a calculation of these electric dipole matrix elements. The overall study predicts an efficient population transfer and provides a time scale for the STIRAP pulse sequence that ensures permanence within the adiabatic regime.

3.1 Overview of three- and four-level STIRAP.

For completeness a brief review of three-level STIRAP (Bergmann et al. (1998)) is presented here. Consider a system with three energy levels and two radiation fields. A schematic representation of a system in a ladder configuration is shown in Fig. 5(a). It is assumed that the Stokes radiation field is detuned by Δ_S with respect to the frequency of the dipole allowed transition between levels $|1\rangle$ and $|2\rangle$, and that the pump beam is detuned by Δ_P with respect to the $|0\rangle$ to $|1\rangle$ electric dipole transition. This also implies that the direct $|0\rangle \rightarrow |2\rangle$ transition is forbidden. One can write the Hamiltonian matrix H that describes the time evolution of the system:

$$H = \frac{\hbar}{2}\begin{pmatrix} 0 & \Omega_P(t) & 0 \\ \Omega_P(t) & 2\Delta_P & \Omega_S(t) \\ 0 & \Omega_S(t) & 2(\Delta_P + \Delta_S) \end{pmatrix} \tag{41}$$

where $\Omega_S(t)$ and $\Omega_P(t)$ are, respectively, the Rabi frequencies of the Stokes and pump beams. Furthermore, it will also be assumed that the whole system is in resonance, that is, $\Delta_P = -\Delta_S$. The time dependent Schroedinger equation reads

$$i\hbar\frac{\partial\vec{c}}{\partial t} = H\vec{c} \tag{42}$$

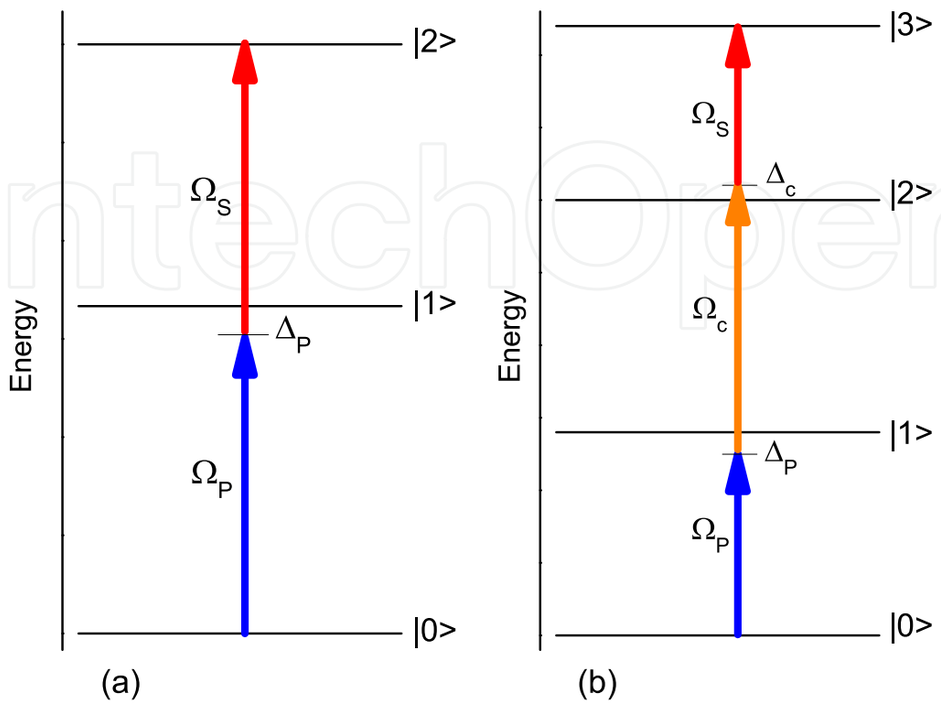

Fig. 5. Schematic representation of a STIRAP process. (a) Three-level STIRAP; (b) four-level STIRAP.

The vector $\vec{c}$ is formed with the expansion coefficients of the state under consideration. We seek a solution to this equation that allows an efficient transfer of population between the initial and final states.
If the time variation of the radiation fields is slow enough the process satisfies the adiabatic condition (Bergmann et al. (1998)) the coefficient vector $\vec{c}$ is an instantaneous eigenvector of the Hamiltonian matrix (41). A direct calculation gives the following eigenvalues for the Hamiltonian:

$$\omega^{+} = \Delta_P + \sqrt{\Delta_P^2 + \Omega_S^2 + \Omega_P^2}$$

$$\omega^{-} = \Delta_P - \sqrt{\Delta_P^2 + \Omega_S^2 + \Omega_P^2}$$

$$\omega^{0} = 0 \tag{43}$$

The eigenstate that corresponds to the last eigenvalue is:

$$\left|v^0\right\rangle = \cos\theta\,|0\rangle - \sin\theta\,|2\rangle \tag{44}$$

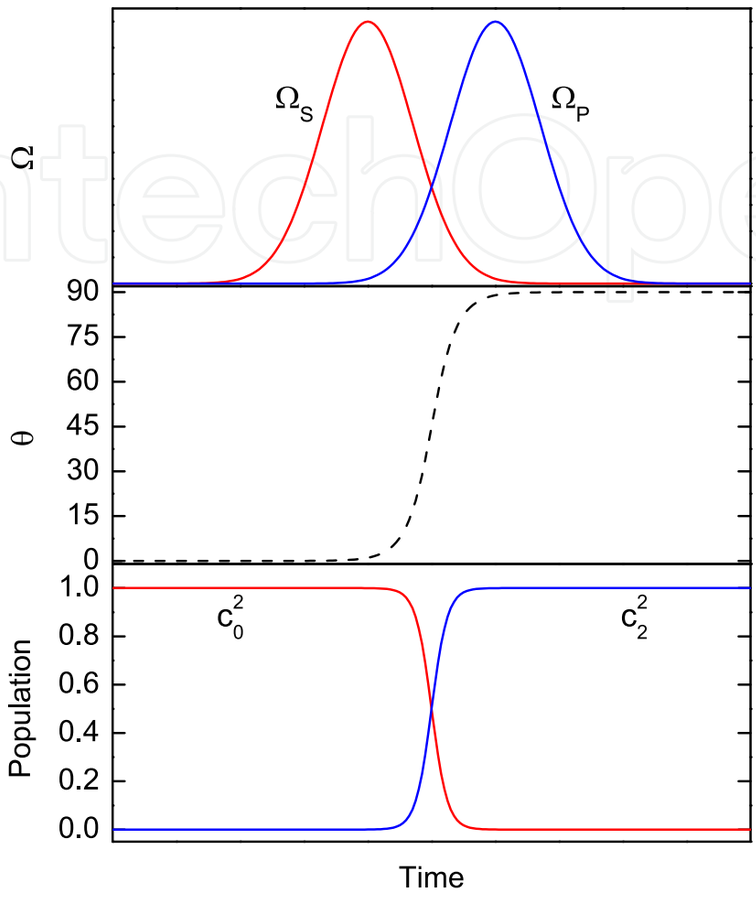

Fig. 6. Pulse sequence (top), mixing angle (middle) and state populations (bottom) in a three-level STIRAP process.

and it is the only one that at all times has no component of the intermediate state $|1\rangle$. The time dependent mixing angle is

$$\tan\theta = \frac{\Omega_P(t)}{\Omega_S(t)} \tag{45}$$

It is now clear that by using light pulses in a sequence in which the Stokes pulse precedes the pump pulse, the mixing coefficient can be varied continuously between 0 and $\pi/2$ and therefore the atomic population can be completely transferred from state $|0\rangle$ to state $|2\rangle$, without ever passing through the intermediate state. This pulse sequence and its effect in the mixing coefficients are graphically represented (Bergmann et al. (1998)) in Fig. 6.
For the system to remain in the dark state throughout the pulse sequence it is necessary that the projection of the rate of change of the expansion coefficient $\vec{c}_0$ onto the other states is small

compared to the difference in eigenvalues (Bergmann et al. (1998)):

$$\left| \frac{d\vec{c}_0}{dt} \cdot \vec{c}_{\pm} \right| << \left| \omega^{\pm} - \omega^0 \right| \tag{46}$$

The extension of STIRAP to systems with more than three levels has also been discussed extensively (Bergmann et al. (1998); Oreg et al. (1992); Smith (1992); Vitanov (1998); Vitanov et al. (1998)). In the case that the intermediate state detunings are zero the behavior of systems with an odd number of states is similar to the one already discussed (Smith (1992); Vitanov (1998)). The Hamiltonian matrix always has a zero eigenvalue and its eigenvector contains only even states in our notation (Smith (1992)). Before all pulses are turned on the corresponding eigenvector is equal to the initial state, and it evolves into the target state as the pulse sequence is applied. The process is robust, in the sense that adiabatic passage is not very sensitive to the detailed forms and delays between pulses, as long as the first and last ones are applied in the counter-intuitive order.

The situation is quite different for an even level system (Oreg et al. (1992); Smith (1992); Vitanov (1998)). There is no adiabatic channel for zero intermediate detunings. In the general case the Hamiltonian matrix has no zero eigenvalue, but it is possible to establish conditions that lead to an eigenstate for adiabatic population transfer (Vitanov (1998)). The conditions require intermediate detunings different from zero and the scheme now depends on the actual pulse sequence because the populations of the intermediate states are different from zero. If the intermediate states can decay by spontaneous emission they may leak population out of the STIRAP process.

Four state STIRAP, shown schematically in Fig. 5(b), is particularly interesting to test these ideas. The Hamiltonian matrix for the system is:

$$H = \frac{\hbar}{2} \begin{pmatrix} 0 & \Omega_P(t) & 0 & 0 \\ \Omega_P(t) & 2\Delta_P & \Omega_c(t) & 0 \\ 0 & \Omega_c(t) & 2\Delta_c & \Omega_S(t) \\ 0 & 0 & \Omega_S(t) & 0 \end{pmatrix} \tag{47}$$

Here Ω_c is the Rabi frequency of a laser that couples the intermediate states $|1\rangle$ and $|2\rangle$ and is detuned from resonance by Δ_{12}. Also, the intermediate detuning $\Delta_c = \Delta_P + \Delta_{12}$ and the assumption is made of overall resonance. This Hamiltonian allows a rather complicated general analytic solution (Oreg et al. (1992)). However, a much simpler condition for the existence of an adiabatic channel can be obtained (Vitanov (1998)). The condition can be extended to general n-level STIRAP processes (Vitanov (1998)). In the case of four levels it is directly expressed in term of the frequency detunings as $\Delta_P \Delta_c > 0$. Therefore, an adiabatic channel exists if there are nonzero intermediate detunings that satisfy this condition (Vitanov (1998)).

Among the schemes proposed for four-level STIRAP there is the production of an intermediate dressed state through the resonant coupling of states $|1\rangle$ and $|2\rangle$ (Smith (1992); Vitanov (1998); Vitanov et al. (1998)). In this case, it is convenient to make $\Delta_{12} = 0$ and the condition for existence of an adiabatic channel, $\Delta_P^2 > 0$ is met as long as the pump beam (and therefore the Stokes beam) is detuned from resonance. It is assumed that the Stokes and pump lasers are turned on in the counter-intuitive sequence while the the coupling laser intensity does not vary in time. Also, to reduce the population of the intermediate states the coupling laser

intensity is assumed much larger than both Stokes and pump laser intensities. In order to propose a model for adiabatic population transfer in rubidium it is important to use sensible values for the Hamiltonian parameters. Among them, the Rabi frequencies of the three steps play a significant role. The pump and coupling pulses connect, respectively, the 5s to the $5p_{3/2}$ and the $5p_{3/2}$ to the 5d states. Both transitions are easily saturated with extended cavity diode lasers. We will therefore assume that Ω_P can be controlled to make it comparable to Ω_S, and that Ω_c can be made several times larger than Ω_P. Thus, we must obtain reasonable values for Ω_S.

3.2 Calculation of 5d→nℓ transition matrix elements.

Rabi frequencies are the product of an electric dipole transition matrix times the electric field amplitude (Metcalf & van der Straten (1999)):

$$\hbar\Omega = \mu_{12}E(t). \tag{48}$$

The electric dipole matrix element μ_{12} is also a product of a geometric factor times the radial matrix element

$$r_{n\ell,n'\ell'} = \int_0^\infty P_{n\ell}(r) r P_{n'\ell'}(r) dr \tag{49}$$

where $P_{n\ell}(r)$ and $P_{n'\ell'}(r)$ are, respectively, the radial wave functions of the initial and final states.

A standard procedure to numerically calculate radial wavefunctions for the valence electron of alkali atoms uses the Numerov algorithm (Gallagher (1994); Zimmerman et al. (1979)). It requires knowledge of the electron potential and the level energy. Starting at large values of r it recursively generates numerical values of the radial wave function for a logarithmic radial mesh. If it is simultaneously applied to initial and final wave functions it allows a direct evaluation of the radial integral. This procedure was used to calculate radial matrix elements for transitions into ns and nd Rydberg states starting from the $5p_{3/2}$ state (Cubel et al. (2005); Deiglmayr et al. (2006); Saffman et al. (2010)). The resulting transition matrix elements were found to be in good agreement with measurements of the Rabi frequencies through the Autler-Townes splitting induced in the lower transition by the upper laser in a two-photon experiment (Cubel et al. (2005); Deiglmayr et al. (2006)).

We followed the same procedure to calculate the Rydberg radial integrals originating in the 5d state. For the Numerov algorithm we used a model potential for alkali atoms (Marinescu et al. (1994)) and the energy levels obtained from a quantum defect analysis (Gallagher (1994); Lorenzen & Niemax (1983)). For comparison we also calculated radial integrals between the $5p_{3/2}$ and the ns, np Rydberg states, with n ranging between 32 and 64. The results are shown in Fig. 7, where we only plot the absolute values of the radial integrals. For each individual series we fitted power expressions of the form $C_\ell \times n^{*-3/2}$, where $n^* = n - \delta_{n\ell}$ is the effective principal quantum number (Gallagher (1994); Lorenzen & Niemax (1983)). The results for the coefficients C_ℓ are shown in Table 1. Our values for the ns and nd series are in good agreement with the previous calculations (Deiglmayr et al. (2006); Saffman et al. (2010)). As expected, our results show that transitions originating from the 5d state have larger radial integrals compared to the transitions originating from the $5p_{3/2}$ state. The C_p coefficient is a factor of 1.9 larger than C_s, and C_f is a factor of 3.1 larger than C_d.

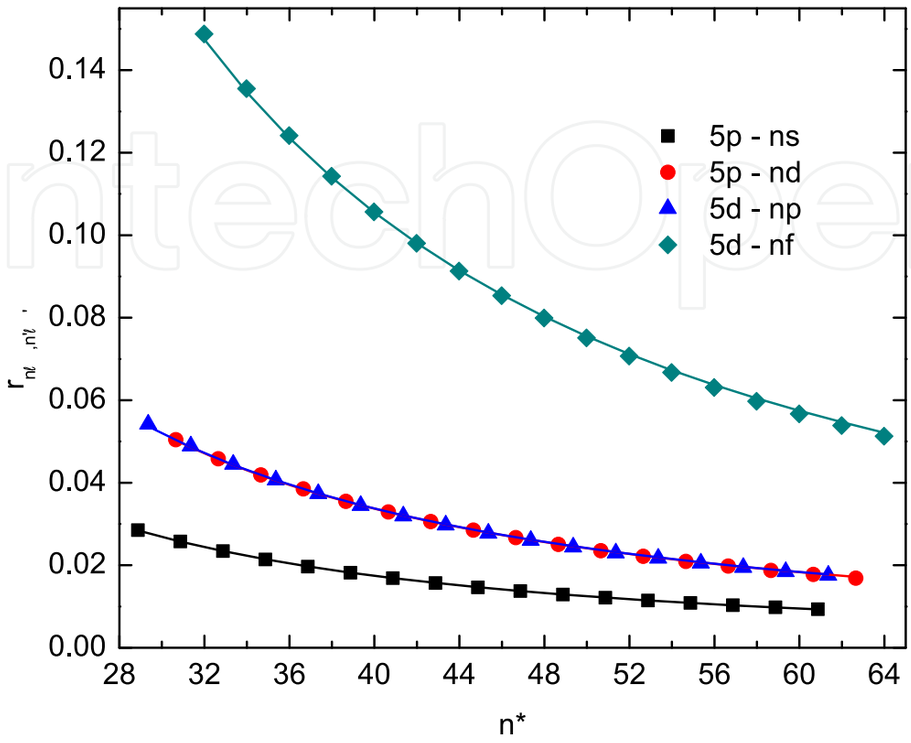

Fig. 7. Results for the absolute values of the $5p_{3/2} \rightarrow n\ell$ and $5d \rightarrow n\ell$ electric dipole radial matrix elements. The symbols are the results of the calculation and the continuous lines are $n^{*-3/2}$ power fits (for details see text).

Rydberg series	$5p_{3/2} \rightarrow ns$	$5p_{3/2} \rightarrow nd$	$5d \rightarrow np$	$5d \rightarrow nf$
Coefficient/a_0	C_s	C_d	C_p	C_f
This work	4.414	8.521	8.537	26.692
Deiglmayr et al. (2006)	4.508	8.475		
Saffman et al. (2010)	4.950	8.485		

Table 1. Results for coefficients C_ℓ of Rydberg radial integrals.

3.3 Four-level STIRAP to produce cold Rydberg rubidium atoms.

Three-level STIRAP has already been used to coherently produce Rydberg states in cold rubidium atoms (Cubel et al. (2005); Deiglmayr et al. (2006)). The atomic states are the 5s, $5p_{3/2}$ and ns or np, and the wavelengths of the pump and Stokes lasers are, respectively 780 nm and 480 nm. Because of its small dipole matrix element, the transition between the $5p_{3/2}$ intermediate state and the target Rydberg level usually requires a high intensity Stokes laser tightly focused into the atomic cloud (Cubel et al. (2005); Deiglmayr et al. (2006)). Recently it was shown (Thoumany et al. (2009)) that continuous excitation of Rydberg states in a vapor cell can be achieved using three relatively inexpensive diode lasers, connecting the $5s \rightarrow 5p_{3/2} \rightarrow 5d \rightarrow np$ or nf ladder sequence. Their wavelengths are, respectively, 780 (pump),

776 (coupling) and about 1259 (Stokes) nm.[1] Also, a three-photon process has the added advantage of being able to excite into Rydberg states of higher orbital angular momentum nf. For the four-level STIRAP calculation we consider the time dependent Stokes and pump fields

$$\Omega_S(t) = \Omega_S^0 \exp\left[-(t-\tau_S)^2/T^2\right]$$
$$\Omega_P(t) = \Omega_P^0 \exp\left[-(t-\tau_P)^2/T^2\right] \tag{50}$$

where both pulses have the same width at half maximum $T^* = 2\sqrt{\ln(2)}T$. For convenience the time scale will be expressed in terms of this pulse width. If one uses the times

$$\tau_S = -\frac{\tau}{2} + \frac{T^2}{2\tau}\ln\frac{\Omega_P^0}{\Omega_S^0}$$
$$\tau_P = \frac{\tau}{2} + \frac{T^2}{2\tau}\ln\frac{\Omega_P^0}{\Omega_S^0} \tag{51}$$

then the origin of the time scale occurs when the two pulses cross, and they are are separated a delay τ. Furthermore, for three level STIRAP it was found that the optimum pulse separation is equal to the pulse width ($\tau_S + \tau_P = T^*$) (Gaubatz et al. (1990)). The coupling field Ω_c will be assumed to be on resonance ($\Delta_{12} = 0$), its amplitude to remain constant throughout the STIRAP process, and its value to be larger than both Ω_S^0 and Ω_P^0. This constant coupling field *dresses* states $|1\rangle$ and $|2\rangle$, producing frequency shifts of $\pm\Omega_c/2$ (Vitanov et al. (1998)). The only entry left in the Hamiltonian matrix (Eq. 47) is the frequency shift Δ_P. It will be taken sufficiently close to $\Omega_c/2$ so that the pump step is nearly resonant with one of the dressed states. This will have the effect of moving one of the eigenstates out of the picture and the system to behave as in three-level STIRAP.

The Rabi frequencies chosen for these simulations are shown in Table 2, where we also give the values of the transition matrix elements and the required laser power densities. The Rabi frequency can be expressed in terms of the power density I as (Metcalf & van der Straten (1999))

$$\frac{\Omega}{2\pi} = \mu_{12}\sqrt{\frac{2I}{\epsilon_0 c h^2}} \tag{52}$$

where ϵ_0 is the vacuum permitivity, c is the speed of light and h is Planck's constant. For the upper 5d$\rightarrow$ nf transition matrix element we use the transition matrix element to produce the state with $n = 50$. Two cases are presented. In case A the Rabi frequency of the Stokes pulse is approximately equal to the Rabi frequency for the $5p_{3/2} \rightarrow$45s transition studied by Deiglmayr et al. (Deiglmayr et al. (2006)). The gain in the transition matrix element reduces the required laser power density and puts the experiment within reach, even using a relatively low power diode laser. The Rabi frequency of the pump field was made equal to twice Ω_S^0 and there should be no major requirements in terms of the laser power density. The coupling field Rabi frequency is about three times Ω_P. It can also be obtained from a diode laser, and its power density means that some focusing will be required. In case B the Rabi frequencies of both Stokes and pump pulses are equal, both within reach of our laboratory. It will be shown later that this symmetric configuration simplifies the analysis of the time dependent

[1] The actual wavelength of the Stokes laser depends of the target Rydberg state.

Rabi frequency	$\Omega_S^0/2\pi$	$\Omega_P^0/2\pi$	$\Omega_c/2\pi$
μ_{12}/a_0	.075	5.1	2.1
Case A	15 MHz	30 MHz	100 MHz
I (W/m^2)	3.6×10^5	2.8×10^2	1.9×10^4
Case B	25 MHz	25 MHz	100 MHz
I (W/m^2)	1.0×10^6	1.9×10^2	1.9×10^4

Table 2. Parameters used in the STIRAP simulations.

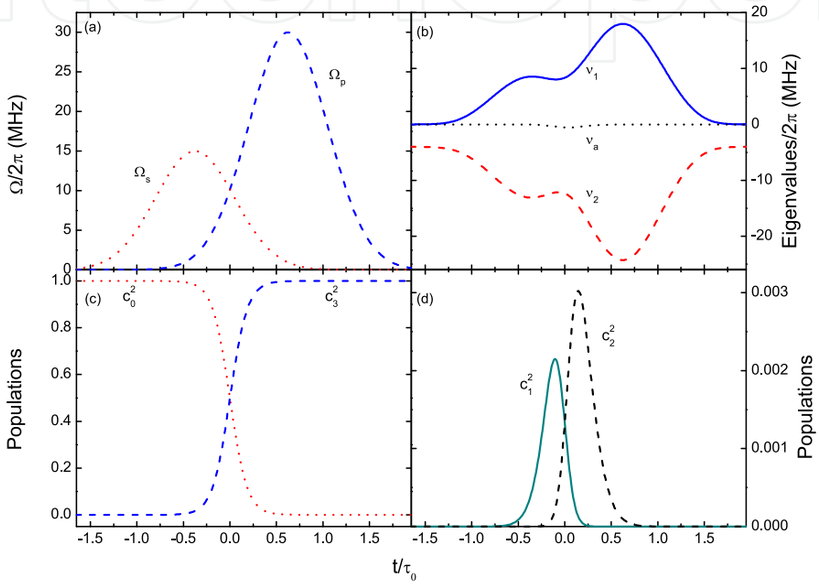

Fig. 8. Results of the simulation of four-level STIRAP for case A. We took equal widths for both Stokes and pump pulses. The pulse delay is equal to the pulse width. (a) pulse sequence; (b) adiabatic eigenvalues ν_0 and its closest eigenvalues ν_1 and ν_2; (c) populations of the adiabatic channels; (c) populations of the intermediate states.

condition for adiabatic following. In both cases the frequency shift $\Delta_P = 48$ MHz, which is slightly smaller than $\Omega_c/2$.

For both cases the eigenvalues and eigenvectors of the Hamiltonian matrix (Eq. 47) were calculated. The adiabatic state corresponds to the eigenvalue that during the STIRAP process is closest to zero. The result of the calculation is shown in Fig. 8 for case A, and in Fig. 9 for case B. The figures include plots of the pulse sequence, with the Stokes pulse preceding the pump pulse, of the three closest eigenvalues and of the populations of the adiabatic state. The eigenvalues show the same qualitative behavior. The adiabatic eigenvalue ω_0 and one of the other eigenvalues (ω_1) tend to zero for large times both before and after the STIRAP process. The other eigenvalue (ω_2) tends to a constant, negative value. Both cases clearly show an adiabatic population transfer between states $|0\rangle$ and $|3\rangle$. But unlike in tree-level STIRAP, there is a small transient population in the intermediate levels $|1\rangle$ and $|2\rangle$. In both cases these transient populations are under 0.004 and last only one pulse width T^*.

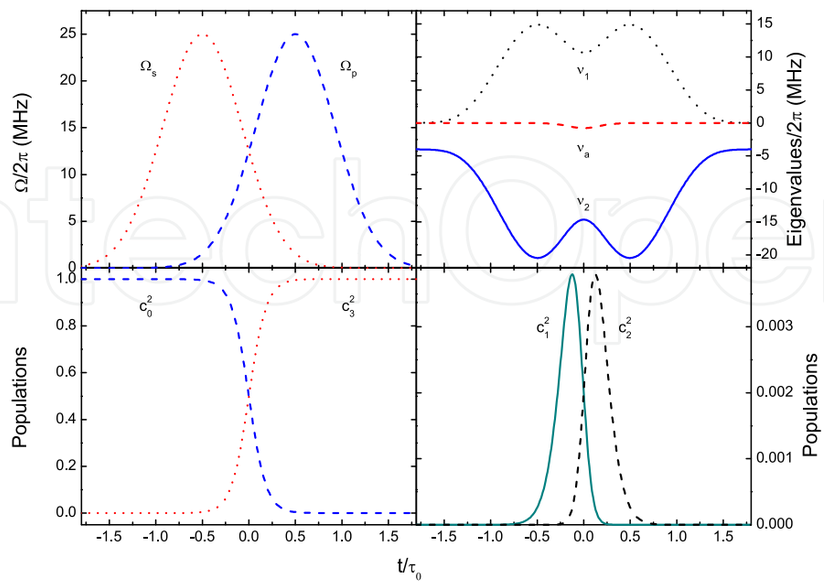

Fig. 9. Results of the simulation of four-level STIRAP for case B. We took equal Rabi frequencies and widths for both Stokes and pump pulses. The pulse delay is equal to the pulse width. (a) pulse sequence; (b) adiabatic eigenvalue ν_0 and its closest eigenvalues ν_1 and ν_2; (c) populations of the adiabatic channels; (c) populations of the intermediate states.

A detailed analysis of the effect of the pulse delay τ in both intermediate state population and the condition for adiabatic following (see below), indicates that the optimum pulse sequence corresponds, as in the three-level case, to $\tau = T^*$. Also, the separation of the adiabatic eigenvalue to the other two eigenvalues, which is one of the determining factors of the adiabatic condition, is largest for $\Delta_P = \Omega_c/2$. For larger values of Δ_P the adiabatic condition severely worsens. However, the numerical analysis is complicated for this value of the shift because the other two eigenvalues start to cross. We found that for values of Δ_P between 30 and 49 MHz we obtained reasonable conditions for adiabatic transfer and at the same time the transient populations of the intermediate states remained small.
Recalling that our unit of time is a pulse width allows us to write the time dependent adiabatic condition as:

$$A_j = \left| \frac{d\vec{c_0}}{dt} \cdot \vec{c}_j \right| \times \left| \omega_0 - \omega_j \right|^{-1} << T \tag{53}$$

where the projection is made onto the non-adiabatic eigenstates. To calculate A_j a numerical time derivative of the adiabatic eigenvector was projected onto the other eigenstates. The results for both case A and case B are shown in Fig. 10. In both cases the curves for A_1 and A_2 have a local maximum close to $t = 0$. However, the projections A_1 have large contributions towards the wings. This occurs because in both $t \to \pm\infty$ limits the adiabatic eigenvalue ω_0 and the nearest eigenvalue ω_1 both tend to zero and the denominator in Eq. (53) rapidly becomes smaller than the numerator.

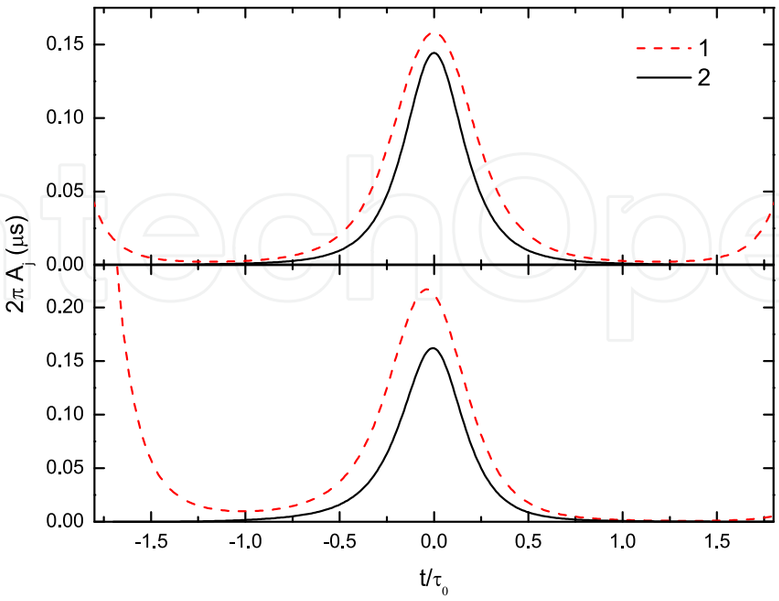

Fig. 10. Time dependent adiabaticity criteria (Eq. 46) for the two closest eigenvalues. Upper panel: case B; lower panel: Case A.

The adiabatic ratio is thus an indication of the time scale of the transfer process. In order to analyze the best conditions for adiabatic transfer one has to consider, on the one hand, the adiabatic condition, an on the other the population of the intermediate, short-lived states. It is convenient to have small values of the adiabatic ratio A_j so that the time scale of the whole process is small, comparable to the shortest lifetime in the system. It is also desirable to have small values for the intermediate state populations. These two quantities depend on the delay between pulses τ. We calculated the adiabatic ratio A_j as function of both time and delay. We took as an indication of the population of the intermediate states the sum of coefficients $c_1^2 + c_2^2$ that also depends on the delay τ. Contour plots for these two quantities are shown in Fig. 11. Both plots were obtained for case B, in which the Rabi frequencies of both Stokes and pump pulses are equal. Similar behavior was found for case A. For low values of the delay the adiabatic ratio near $t = 0$ takes the smaller values and the contribution from the wings is largest. As the delay increases the wing contribution diminishes, but now the values near $t = 0$ start to grow. At the upper end, near $\tau = 1.5$ the adiabatic ratio at $t = 0$ is close to one, and this would impose the need for transfer times that are much larger than the intermediate state lifetime. The behavior of the intermediate state population sum is the opposite. It takes its largest value, close to 0.1 for small delays, and then it decreases. The condition $\tau = T$ is the one that results in small enough values of A_j and at the same time small intermediate state populations. This is precisely the condition that was used to obtain figures 8 and 9. Thus one can use the adiabatic ratios in Fig. 10 to obtain the condition for the pulse width

$$T >> \frac{0.16}{2\pi}\ \mu s \tag{54}$$

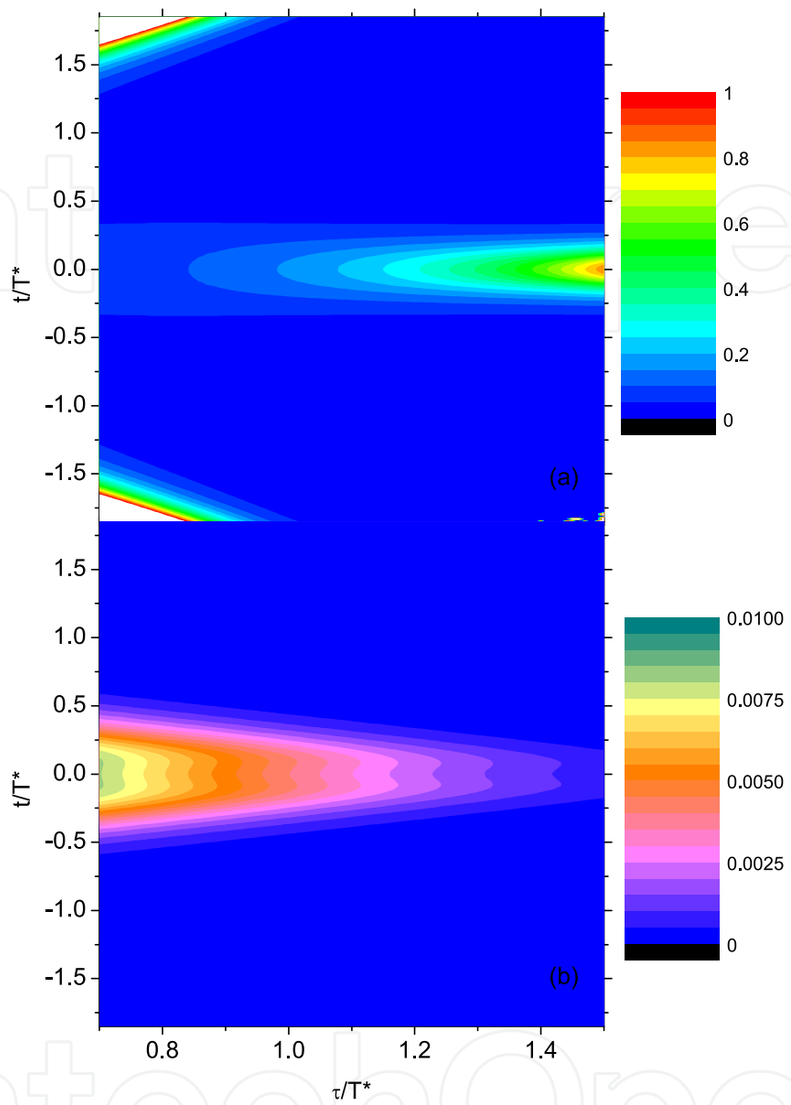

Fig. 11. Adiabatic ratio (top) and populations of the intermediate states as functions of time and delay between pulses. These plots correspond to case B. The abscissae correspond to reduced delay τ/T and the ordinates to the reduced time t/T in the pulse sequence.

This is satisfied with 500 ns pulses which are about a factor of 20 longer than the lifetime of the $5p_{3/2}$ state. At the same time it is possible to obtain them in the laboratory using standard acusto-optic modulators.

3.4 Summary

In summary, in this section we presented a calculation of the 4-level STIRAP process to efficiently transfer population between the 5s ground state in rubidium to nf Rydberg states. The transition matrix elements between the second intermediate state 5f and the Rydberg state

result in a gain of a factor of 3 in the Rabi frequency. The whole process should be possible in the laboratory, with commercial diode lasers and in time scales that are at the same time attainable with acusto-optic modulators and not much longer than the shortest lifetime in the four level system.

4. Laser interactions with glow plasmas

Low temperature (2-20 eV in electronic temperature) plasmas provide one of the richest natural sources of radical, excited, neutral, metaestable and clustered atomic and molecular species Marcus &Broekaert (2003). When a laser pulse is made to interact with a plasma of these characteristics, practically any of the processes allowed by molecular or atomic selection rules may take place within the plasma. In this respect, a plasma-laser experiment provides, in an integrated fashion, a very comprehensive set of possibilities to study molecular processes in a single experimental set up. In these experiments one may study and quantify processes such as electron photo-detachment of anions, photo-ionization of metastable states, molecular predissociation and resonant excitation of short lived species. This serendipity provided by plasma laser interaction is hampered, however, by the fact that these processes take place simultaneously within a relatively dense medium. For this reason, it takes some ingenuity to extract and unravel a specific part of information and to make quantitative assessment of a particular process induced by the laser Baribieri et al. (1990). A well established technique that has been used for many years to extract spectroscopic information from plasma-laser interactions is the optogalvanic effect (OGE). In this section a brief on the fundamental characteristics and features of the optogalvanic process will be presented. In addition to this, a discussion on the fundamental processes which give rise to impedance changes within the plasma, as induced by laser light will be commented upon. Based on this basic principles, both the slow and fast optogalvanic effects will be presented and described. Since the slow optogalvanic effect has been studied and used for many years, the focus of the examples on applications in this section will be devoted to the fast optogalvanic effect. To illustrate the power and versatility of the fast optogalvanic effect, an example on the study of atomic photoionization from metastable states will be discussed. The final part of this section will be devoted to outlining the recent trends in optogalvanic studies, especially those related to applied use of novel light sources in the mid infrared spectral ranges. Some selected actual and potential applications in biology as well as the most salient applications in medicine will be presented, as derived from OGE studies.

4.1 The Optogalvanic effect (OGE)

The optogalvanic effect was first observed (Penning, 1926) when, during the observation of the current characteristics of a neon discharge, a change in the impedance was observed when irradiated by an emission of a nearby neon discharge. However, systematic, extensive and practical applications of this interesting effect were only possible when tuneable dye lasers were available in the decade of 1960. In 1970 the technique was mature enough to allow studies of electron excitation from metastable states with high resolution (Green et al. (1980)) and the spectroscopic studies of refractory elements in hollow cathode discharges. Incidentally, the study of refractory elements had been hampered in the past due to the need of complex ovens of high temperatures. Plasmas in hollow cathode discharges provide a good source of refractory materials in the gas phase as these species are produced with

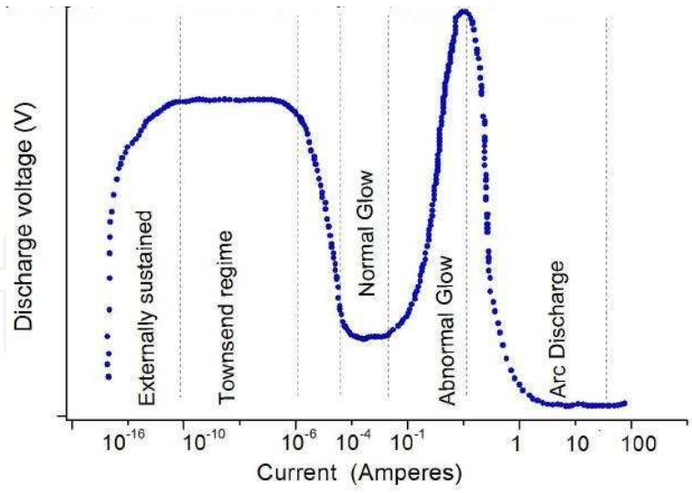

Fig. 12. Voltage current curve illustrating the different discharge regimes that may occur in a gaseous discharge, as a function of the discharget's current.

ion sputtering processes, within the discharge. The technique has grown stronger with the coming decades and is now widely used in a wide range of applications ranging from trace gas detection, studies of autoionizing states, isotopic ratio analysis, and laser stabilization applications, to name just a few.

The optogalvanic effect consists, briefly, in a change of the conductivity properties of a plasma, as induced by a pulse of electromagnetic radiation. This change in conductivity may be incremental or decremental, and presents a strong dependence with wavelength. In addition to this, the OGE can be fast, i.e. the conductance changes are as fast as the exciting laser pulse width, or slow, where the response can be 2 or 3 orders of magnitude slower than the exciting laser pulse. Before presenting a brief description of this process, it is convenient to revise briefly the basics of steady low-pressure gaseous discharges. Gas discharges can be separated in different regimes according to the voltage-current characteristic curve presented in Fig. 12. Although the optogalvanic effect has been observed both in the Townsend region (Kravis & Haydon (1981)) and in the arc region the most interesting and relevant studies have been carried out in the normal glow discharge. This is in part due to the fact that the geometry of a discharge in the glow regime is well established and can be understood based on simple atomic collision models.

Figure 13 shows the typical layout of a glow discharge between parallel plates. This schematic representation corresponds to a direct-current discharge in a tube filled with a rare gas, in a pressure range between 0.1 to 1 Torr. The physical explanation of these differentiated regions can be consulted in depth elsewhere (Engel (1965)). For the slow optogalvanic effect, the most relevant region corresponds to the positive column. The slow response of the conductivity changes as compared to the pulse width occur if the laser pulse is focused in this region. In this region, the axial component of the electric field is nearly constant and several orders of magnitude smaller as compared to that of the dark space. The fast optogalvanic effect takes place if the laser is focused in the small region depicted in Fig. 13 and labeled as the Aston space. This region is characterized by the fact that the largest electric field gradient takes place in this region. In this region, the presence of a bimodal electron energy distribution of electrons slowed by inelastic collisions with the gas, and fast electrons whose energy is too

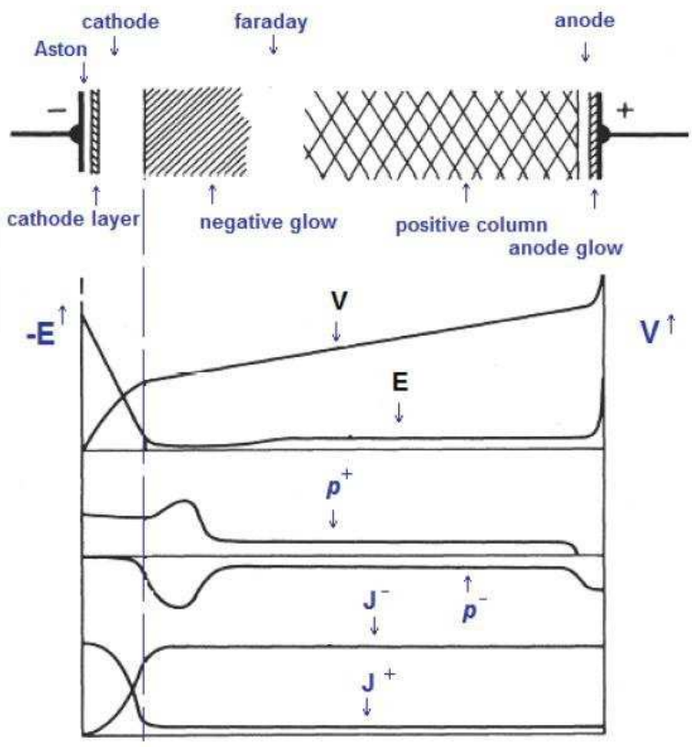

Fig. 13. Spatial distribution of a discharge between two parallel plates in the glow regime. The upper figure shows the electric field (E) distribution, space charge ρ^+, ρ^- and current densities J^+ and J^-.

high to contribute to the electron impact cross section. The above mentioned characteristic is the responsible for the differences in time response of the slow and fast optogalvanic effects. The fast optogalvanic effect has its origin in photoionization events. Due to the bimodal structure of the electron energy distribution, this region is rich in excited states. A laser pulse, even in the visible energy range, can induce a transition from one of these excited states into the continuum. Due to the high electric field present in the Crookes space, any photoelectron produced induces the production of a cascade of electrons in a nanosecond time scale. The slow optogalvanic process, on the other hand, is due to the resonant absorption of light, and its subsequent conversion of electromagnetic energy into kinetic energy. This conversion is mediated by super-elastic collisions which transfer the internal energy of the photon, molecule or radical, into kinetic energy. The scale of time for the propagation of the slow OGE is of the order of micro or milliseconds, depending on the size and geometry of the vessel containing the discharge. Experimentally, the simplest set up required to carry out optogalvanic measurements is depicted in Fig. 13.

In its simplest case, the experimental arrangement to measure optogalvanic transitions in plasmas is depicted in Fig. 14. A CW laser, tunable in wavelength is modulated in intensity with a mechanical chopper. The modulated light source is made then to interact with a discharge in the normal glow regime, either in the positive column or close to the Aston dark space. The variations in the plasma current is recorded with a phase sensitive lock in amplifier. These variations are recorded as a function of wavelength and the resulting spectrum can then

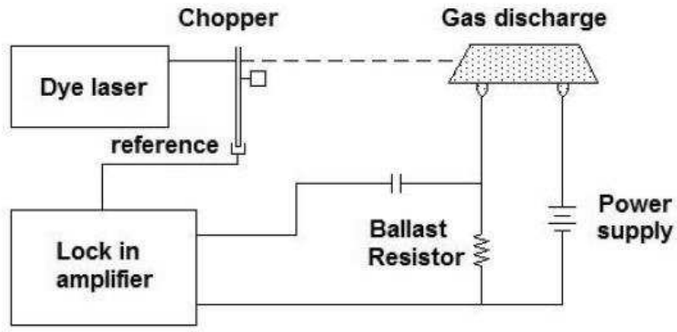

Fig. 14. Schematic of the most basic experimental arrangement required to carry out optogalvanic measurements. Most advanced schemes include a pulsed laser source and a boxcar integrator.

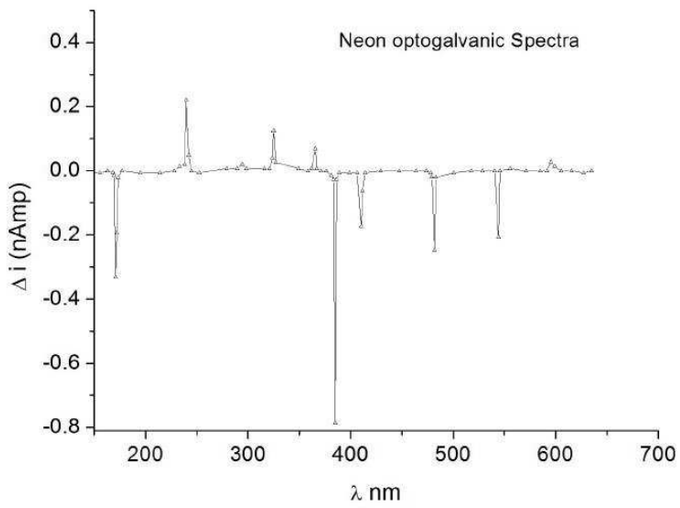

Fig. 15. Experimental optogalvanic spectra of neon illustrating the decrease and increase of conductivity (hence of current) as a function of wavelength.

be analyzed. A spectra of the optogalvanic effect in neon, as obtained with such a simple experimental arrangement is shown in Fig. 15.

In figure 15 one may notice a characteristic feature of the optogalvanic effect: the current can vary positively or negatively. The increase is possible because the resonant interaction of light with the plasma may increment both the density of ionized atoms or molecules and the increase in conductivity due to inelastic transfer of light to atomic or molecular kinetic energy. The decrease is usually produced by the quenching on the metastable population due to optical pumping, followed by optical emission in a cascade of dipole allowed transitions down to the ground state. This quenching effectively decreases the density of ionized targets and, hence the resonant transfer of electromagnetic energy into heat or ion electron pairs. This latter effect is, in turn reflected on the decrease of current as a function of wavelength of the laser light.

4.2 Photoionization studies with the Fast OGE

The use of Resonance Ionization Spectroscopy (RIS) has been very useful in the study of several interesting physical processes. With this technique it has been possible to study highly excited Rydberg states (Babin & Gagné (1992) and references therein), carry out isotopic effect studies and isotope separation (Letokhov & Chebotayev (1977)) and reach the single atom detection limit (Hurst et al. (1979)). However, the usefulness of this powerful technique is hampered by the need of a relatively complex experimental arrangement. The use of RIS usually requires the availability of an atomic or molecular beam two or more laser systems to reach intermediate resonance states prior to ionization and fast charged particle detectors to obtain the photoion or photoelectron yield as a function of wavelength. The fast optogalvanic effect (FOGE) may offer an interesting alternative to these techniques, with the advantage over the previously mentioned RIS techniques of its inherent experimental simplicity. The FOGE method was initiated with the observation of (Broglia et al. (1987)), of a rapid optogalvanic signal 10^{-10} s in the dark space of a hollow cathode discharge (HCD). This fast pulse arises solely from photoionization events which take place in the Aston dark space. In this scheme, the discharge is used as a photoelectron detector as well as a neutral atomic vapor generator via cathodic sputtering and is thus particularly appropriate to the study of refractory elements. The FOGE scheme has been used to study high resolution photoionization transitions of uranium (Gagné et al. (1983)) and to carry out fundamental studies of the dark space properties of a hollow cathode (Babin & Gagné (1992)) as well as the photoionization spectroscopy of the copper atom (Widiger et al. (1994)). The value of this method is its capability of measuring the photoionization cross section as well as the volume density of the initial state of the sample under study. This can be obtained directly from the time dependent quantification of the evolution of the fast optogalvanic signal generated in the discharge Aston dark space (Stockhausen et al. (1996)).

4.2.1 Experimental arrangement of the FOGE

Figure 16 shows a schematic representation of the simplest FOGE set up that can be used to carry out photoionization measurements. In the example shown the laser pulse is produced by a pulsed dye laser pumped with a nitrogen laser, with mean pulse energy and duration of 200 μJ and a pulse width of 5 ns respectively. The beam radius at the waist, positioned in the dark space and grazing the cathode, is 0.17 mm and is focused by a set of cylindrical lenses not shown in the schematic representation. The laser pulse width and energy delivers a fluence of 5 x 10^{25} photons/cm^2/s. The FWHM of the laser is 0.6 cm^{-1}, but this width is not significant as most of the line broadening in the photoionization experiments arises from Doppler broadening. The discharge is maintained with a current-stabilized voltage source, to which we added a 550 ballast resistor mounted in series with the lamp. This resistance value was chosen in order to limit the discharge's current and prevent it from becoming an arc. A 0.1 μF capacitor is connected in parallel with the discharge in order to maintain the voltage drop during the laser pulse. A current divider directs the photoionization current towards a boxcar, which is protected from the high voltage DC of the lamp and high frequency instabilities by a decoupling capacitor and a pair of fast diodes mounted in parallel.

In order to maximize the atomic vapor production, one should keep the gas pressure as low as possible whatever the carrier gas used. Operating the discharge at a high current may cause premature erosion of the cathode and the formation of secondary zones of variable conductivity, which would ruin the stability of the discharge. Recall that the hollow

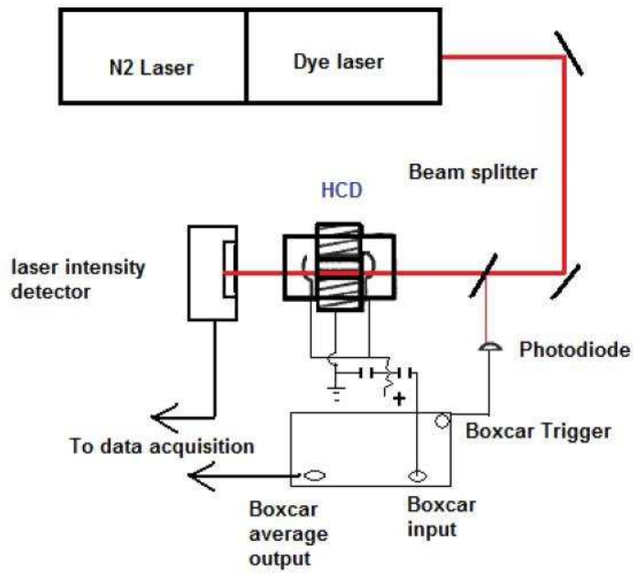

Fig. 16. Experimental arrangement for photoionization measurements employing the Fast Optogalvanic Effect (FOGE). More complex arrangements may involve the use of another laser for ground state pumping used to simplify spectroscopic analysis. HCD stands for Hollow Cathode Discharge.

cathode geometry and the operating conditions must be so that the negative glows overlap in the middle of the discharge. At the same time, the fast electrons accelerated on one side of the hollow cathode and going across the plasma must not strongly perturb the facing dark space. Figure 16 shows the simplest experimental arrangement that can be used for FOGE measurements. One of the most useful uses of the FOGE effect is on the study of photoionization of refractory materials. The usual acronym used for this use of the FOGE technique is PIOG, standing for Photoionization Optogalvanic effect. Fig. 17 shows a part of the PIOG spectrum (Levesque et al. (1997)) recorded using a 150 mTorr Xe discharge. On the same plot a slow optogalvanic effect spectrum is recorded for calibration purposes. The wavelength scale is not shown in the figure but can easily be inferred by using the simultaneously acquired slow optogalvanic spectrum, along with the Fabry- Perot fringes. Instead, the scanning time is recorded in the x axis in order to illustrate that, due to the nonlinear nature of the scanning of the dye lasers, it is convenient to record a Fabry-Perot interferogram along with the PIOG and TOG. Using such a reference, the nonlinear wavelength scanning of the dye laser is evident here. Those scanning speed variations restrict the wavelength calibration reproducibility of the PIOG spectra to 0.3 cm^{-1}. However, when care is taken to minimize these non-linearities with a closed loop positioning control, the PIOG technique can easily yield, on a specific spectrum, consistent from line to line within 0.1 cm^{-1}.

One also observes that the PIOG and TOG spectra are really different. Even though it frequently happens that strong photoionization lines regroup around an intense TOG line, as shown on figure 17 (lines marked A and B), other intense lines are not related to TOG lines, or, if so, to very weak ones, as exemplified by the lines marked C and D. In summary, the

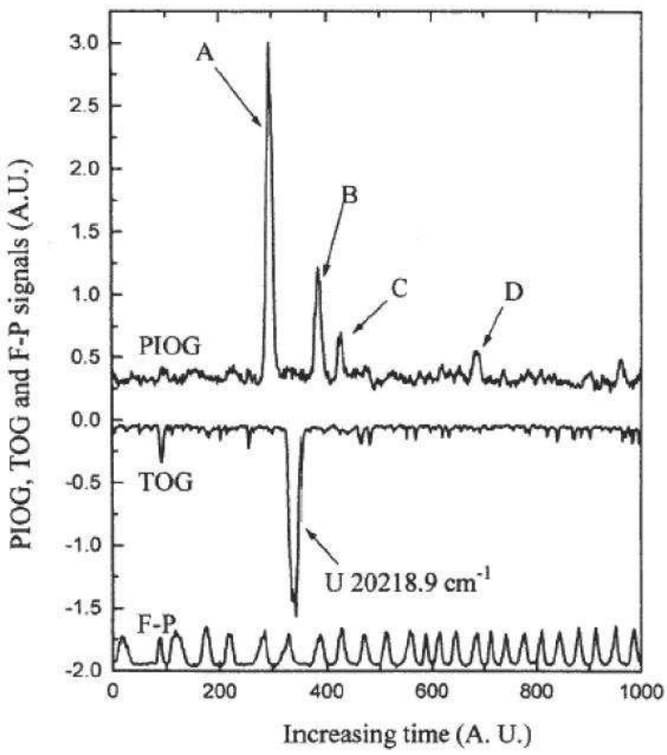

Fig. 17. PIOG Spectra of a Xenon discharge, along with a thermal OGE spectra and Fabry-Perot interferogram. The nonlinear scanning properties of dye lasers are made evident. (with permission from IOP publishing, Levesque et al. (1997))

FOGE technique provides a useful tool to assess the photoionization yield of gas phase and refractory elements, and, combined with other techniques, may yield very useful results.

4.3 New developments and future trends of OGE

The optogalvanic effect and techniques is a relatively old and well established technique. However, with the development of new, simple and affordable light sources of solid state and in wavelengths previously inaccessible, the technique is still producing a wealth of new applications. In this section a brief outline of these new applications and new trends will be presented. One of the most salient features is its great sensitivity. The efficiency of detection of the optogalvanic technique can be very competitive, reaching the part per billion detection level. This technique can then be favorably compared to other trace gas detection alternatives such as Cavity Ring Down, optoacustic spectroscopy or Resonance Ionization spectroscopy. Trace gas sensing, in turn, is of great interest in numerous areas. These include atmospheric chemistry, volcanic activity, agriculture, industrial process and workplace surveillance, gas certification, medical diagnostics, etc. The competence of the OG effect to provide a tool for trace detection allows foreseeing that its use will continue to be intensive in the future.

4.3.1 Laser sources for use with OGE

In the past, the only choice of lasers to implement the OGE and FOGE studies were pulsed N2 or Nd:YAG lasers. With the recent development of external cavity diode lasers, or ECDL,

Laser	wavelength range	Power range
External Cavity Diode Laser	800-1600 nm	1-200 mW
CO laser	2.7-4, 5.1-6, μm	mW-Watt
CO2 laser	9-11 μm	Watt
Lead salt diode	4-30 μm	0.1 mW
Quantum Cascade Laser	4-24 μm	mW
Optical parametric Oscillator	3-16 μm	<1W
Difference frequency generator	3-16 μm	mW

Table 3. Typical ranges and parameters of laser sources available for optogalvanic and spectroscopic studies.

the capabilities and potential of the optogalvanic studies is more appealing today. For mid infrared application there are alternatives provided by quantum cascade lasers, as well as nonlinear optical devices, based on four wave mixing, but operating with very low powers (Markus (2003)). This very recent developments on mid infrared off the shelf optics, based on photonic band gap hollow fibers allow to forecast a very intensive use of the technique in trace detection in the mid infrared. Table 3 briefly summarizes the current situation related to the current accessible wavelengths, tuning characteristics, typical power range, and operation parameters of laser sources available for optogalvanic and spectroscopic studies in general.

4.3.2 Application of OGE spectroscopy in biology and medicine

Trace gas detection is currently a very active area of applied research. With the high sensitivity provided by the optogalvanic spectroscopy, there is a great potential for this technique in the trace gas detection area. In this final part of the section devoted to the OGE some illustrative applications in the area of biology and medicine will be presented. Of particular interest for these applications is the Infrared spectral range. The applications range from the monitoring industrial processes, specially of flames and catalytic reduction of pollutants, to air quality monitoring in great cities, the quantification of CO_2 sinks and sources, to national security to the monitoring of biological processes in living organisms (including the human body). In all of these applications, the use of trace detection spectrometers coupled with laser-based spectroscopic gas are indispensable (Sigrist (2003)). The most intense absorption bands of organic molecules lie in the wavelength region between 2.5 and 20 μm, where these molecules have their fundamental rovibrational transitions. The areas of interest where the optogalvanic spectroscopy could find a future niche will involve the detection of organic molecules which absorb in this range of wavelengths. To be more specific, the detections such as ethylene, methane, CO_2 and CH_4 could open up a wealth of possibilities for the technique (Cristescu et al. (2008)).

In the case of ethylene, it is a well know plant hormone that is conspicuous in many biological processes of the plant and fruits, such as death cell signaling, nitrogen fixation processes, circadian clock system of several plants, molecular alarm systems of fungi infection of fruits and tomatoes and even in the metabolic changes of human physiology induced by the light from the sun (Cristescu et al. (2008)). Acetone is a biomarker the increase of which in the human breath signals the onset of diabetes. A sensitive detector based on optogalvanic spectroscopy to quantify the presence of this molecule would have potentially a great use in hospitals and small clinics (Aman & Smith (2005)). Nitric oxide detection in the part per billion sensitivity could be of great clinical use in the early detection of lung pathologies and

organ rejection monitoring, hepatopulmonary diagnostics, malaria and even gastritis, through the detection of the helicobacter pillory bacteria through its metabolic signature in the human breath. The scope and importance of these applications and several others make the area of research of new OGE detectors and techniques a very promising area of research in the future.

5. Acknowledgments

We knowledge support from grants DGAPA-UNAM IN-116309 (J.J.M.), DGAPA-UNAM IN-101611-3 (R.C.T.), and DGAPA-PAPIIT IN113910 (AMJ).

6. References

Aman, A. & Smith, D. (2005). *Breath Analysis for clinical diagnosis and therapeutic monitoring*, World Scientific Publishing Co. Pte Ltd., Singapore.

Anis, F., Roudnev, V., Cabrera-Trujillo, R. & Esry, B. D. (2006). Laser assisted charge transfer in $He^{2+} \rightarrow H$ collisions, *Phys. Rev. A* 73: 043414.

Babin, F. & Gagné, J. (1992). Hollow Cathode Discharge (HCD) dark space diagnostics with laser photoionization and galvanic detection, *Appl. Phys. B* 54: 35.

Baribieri, B., Beverini, N., & Sasso, A. (1990). Optogalvanic spectroscopy, *Rev. Mod. Phys.* 62: 603.

Bergmann, K., Theuer, H. & Shore, B. W. (1998). Coherent population transfer among quantum states of atoms and molecules, *Rev. Mod. Phys.* 70: 1003 and references therein.

Broglia, M., Catoni, F., Montone, A. & Zampetti, P. (1987). Galvanic detection of laser photoionization in hollow-cathode discharges: Experimental and theoretical study, *Phys. Rev. A* 36: 705.

Cabrera-Trujillo, R. (2009). Laser and isotope effects in charge transfer processes in atomic collisions, *Rad. Effects Defects Solids* 164: 402.

Carroll, C. E. & Hioe, F. T. (1988). Three-state systems driven by resonant optical pulses of different shapes, *J. Opt. Soc. Am. B* 5: 1335.

Copeland, D. A. & Tang, C. L. (1976). Photon-assisted nonresonant charge exchange: A simple molecular model, *J. Chem. Phys.* 65: 3161.

Cristescu, S., Persijn, S., Lintel, H. & Harrend, F. (2008). Laser-based systems for trace gas detection in life sciences, *Appl. Phys. B* 92: 343.

Cubel, T., Teo, B., Malinovsky, V., Guest, J., Reinhard, A., Knuffman, B., Berman, P. & Raithel, G. (2005). Coherent population transfer of ground-state atoms into Rydberg states, *Phys. Rev. A* 72: 023405.

Deiglmayr, J., Reetz-Lamour, M., Amthor, T., Westermann, S., de Oliveira, A. & Weidemüller, M. (2006). Coherent excitation of Rydberg atoms in an ultracold gas, *Opt. Commun.* 264: 293.

Engel, A. v. (1965). *Ionized Gases*, second edition, Claredon, Oxford, England.

Errea, L. F., Méndez, L. & Riera, A. (1983). On laser-induced charge transfer in the HeH^{2+} quasimolecule, *J. Chem. Phys.* 79: 4221.

Ferrante, G., Cascio, L. L. & Spagnolo, B. (1981). Laser-assisted symmetric charge transfer in atomic collisions, *J. Phys. B* 14: 3961.

Gagné, J., Demers, Y., Pianarosa, P. & Dréze, C. (1983). Effet optogalvanique dans une décharge á cathode creuse: Mécanisme et dosage isotopique de l'uranium, *Journal de physique (Paris)* C7-44: 355.

Gallagher, T. (1994). *Rydberg Atoms*, Cambridge University Press, Cambridge, UK.

Gaubatz, U., Rudecki, P., Becker, M., Schiemann, S. & Bergmann, K. (1990). Population transfer between molecular vibrational levels by stimulated Raman scattering with partially overlapping laser fields. a new concept and experimental results, *Chem. Phys. Lett.* 92: 5363.

Gearba, M., Camp, H., Trachy, M., Veshapidze, G., Shah, M., Jang, H. & DePaola, B. (2007). Measurement of population dynamics in stimulated Raman adiabatic passage, *Phys. Rev. A* 76: 013406.

Green, R., Havrilla, G. & Trask, T. (1980). Laser-enhanced ionization spectrometry: Characterization of electrical interferences, *Appl. Spectrosc.* 34: 561.

Gudzenko, L. I. & Yakovenko, S. I. (1972). Radiative collisions, *Sov. Phys. JETP* 35: 877.

Havener, C. C., Rejoub, R., Krstić, P. S. & Smith, A. C. H. (2005). Charge transfer in low-energy collisions of He^{2+} with atomic hydrogen, *Phys. Rev. A* 71: 042707.

Hurst, G., Payne, S., Kramer, S. & Young, J. (1979). Resonance ionization spectroscopy and one-atom detection, *Rev. Mod. Phys.* 51: 767.

Kirchner, T. (2002). Manipulating ion-atom collisions with coherent electromagnetic radiation, *Phys. Rev. Lett.* 89: 093203.

Kirchner, T. (2004). Laser-field-induced modifications of electron-transfer processes in ion-atom collisions, *Phys. Rev. A* 69: 063412.

Kirchner, T. (2005). Pauli blocking and laser manipulation of electron dynamics in atomic collisions, *Nucl. Instr. Meth. B* 233: 151.

Kravis, S. & Haydon, S. (1981). Laser-induced optogalvanic effects under prebreakdown conditions in neon, *J. Phys. D: Appl. Phys.* 14: 151.

Kuklinski, J., Gaubatz, U., Hioe, F. & Bergmann, K. (1989). Adiabatic population transfer in a three-level system driven by delayed laser pulses, *Phys. Rev. A* 40: 6741.

Letokhov, V. & Chebotayev, V. (1977). *Nonlinear Spectroscopy*, Springer Verlag, Berlin.

Levesque, S., Gagne, J. M. & Babin, F. (1997). Optogalvanic photoionization spectroscopy, *J. Phys B: At. Mol. Opt Phys* 30: 1331.

Lorenzen, C.-J. & Niemax, K. (1983). Quantum defects of the $n^2p_{1/2,3/2}$ levels in ^{39}K and ^{85}Rb, *Phys. Scr.* 27: 300.

Malinovsky, V. & Tannor, D. (1997). Simple and robust extension of the stimulated Raman adiabatic passage technique to n-level systems, *Phys. Rev. A* 56: 4929.

Marinescu, M., H.R., S. & Dalgarno, A. (1994). Dispersion coefficients for alkali-metal dimers, *Phys. Rev. A* 49: 982.

Marcus R.K. and Broekaert J.A.C., (2003). *Glow Discharge Plasmas in Analytical Spectroscopy*, John Wiley &Sons, Ltd. ISBN: 0-471-60699-5, London, England

Markus, W. (2003). Trace gas monitoring by laser photoacoustic spectroscopy and related techniques, *Rev. Sci. Instrum.* 74: 486.

Metcalf, H. & van der Straten, P. (1999). *Laser Cooling and Trapping*, Springer, New York.

Oreg, J., Bergmann, K., Shore, B. & Rosenwaks, S. (1992). Population transfer with delayed pulses in four-state systems, *Phys. Rev. A* 45: 4888.

Oreg, J., Hazak, G. & Eberly, J. (1985). Multilevel inversion schemes in and beyond the adiabatic limit, *Phys. Rev. A* 32: 2776.

Oreg, J., Hioe, F. & Eberly, J. (1984). Adiabatic following in multilevel systems, *Phys. Rev. A* 29: 690.

Pindzola, M. S., Minami, T. & Schultz, D. R. (2003). Laser-modified charge-transfer processes in proton collisions with lithium atoms, *Phys. Rev. A* 68: 013404.

Press, W. H., Teukolsky, S. A., T.Vetterling, W. & Flannery, B. P. (1992). *Numerical recipes*, 2nd edition, Cambridge University Press, New York, USA.

Saffman, M., Walker, T. & Molmer, K. (2010). Quantum information with Rydberg atoms, *Rev. Mod. Phys.* 82: 2313.

Sigrist, M. (2003). Trace gas monitoring by laser photoacoustic spectroscopy and related techniques, *Rev. Sci. Instrum.* 74: 486.

Smith, A. V. (1992). Numerical studies of adiabatic population inversion in multilevel systems, *J. Opt. Soc. Am. B* 9: 1543.

Stockhausen, G., Mende, W. & Kocj, M. (1996). Laser-induced photoionization in the dark space of a hollow cathode, *J. Phys B: At. Mol. Opt Phys* 29: 665.

Stolterfoht, N., Cabrera-Trujillo, R., Öhrn, Y., Deumens, E., Hoekstra, R. & Sabin, J. R. (2007). Strong isotope effect on the charge transfer in slow collisions of He^{2+} with atomic hydrogen, deuterium and tritium, *Phys. Rev. Letters* 99: 103201.

Süptitz, W., Duncan, B. & Gould, P. L. (1997). Efficient 5d excitation of trapped Rb atoms using pulses of diode-laser light in the counterintuitive order, *J. Opt. Soc. Am. B* 14: 1001.

Thoumany, P., Germann, T., Hänsch, T., Stania, G., Urbonas, L. & T., B. (2009). Spectroscopy of rubidium Rydberg states with three diode lasers, *J. Mod. Opt.* 56: 2055.

Vitanov, N. (1998). Adiabatic population transfer by delayed laser pulses in multistate systems, *Phys. Rev. A* 58: 2295.

Vitanov, N., Shore, B. & Bergmann, K. (1998). Adiabatic population transfer in multistate chains via dressed intermediate states, *Eur. Phys. J. D* 4: 15.

Widiger, G., Willke, B. & Kock, M. (1994). Laser photoionization of copper atoms in the dark space of a hollow cathode discharge, *J. Phys B: At. Mol. Opt Phys* 27: 899.

Zimmerman, M., Littman, M., Kash, M. & Klepner, D. (1979). Stark structure of the Rydberg states of alkali-metal atoms, *Phys. Rev. A* 20: 2251.

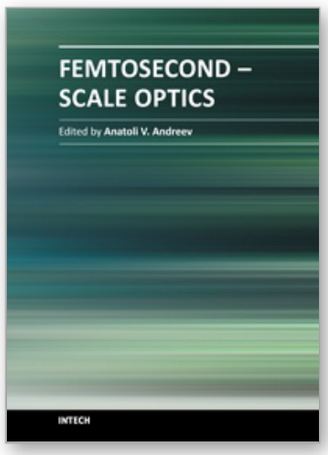

Femtosecond-Scale Optics
Edited by Prof. Anatoly Andreev

ISBN 978-953-307-769-7
Hard cover, 434 pages
Publisher InTech
Published online 14, November, 2011
Published in print edition November, 2011

With progress in ultrashort ultraintense laser technologies the peak power of a laser pulse increases year by year. These new instruments accessible to a large community of researchers revolutionized experiments in nonlinear optics because when laser pulse intensity exceeds or even approaches intra-atomic field strength the new physical picture of light-matter interaction appears. Laser radiation is efficiently transformed into fluxes of charged or neutral particles and the very wide band of electromagnetic emission (from THz up to x-rays) is observed. The traditional phenomena of nonlinear optics as harmonic generation, self-focusing, ionization, etc, demonstrate the drastically different dependency on the laser pulse intensity in contrast the well known rules. This field of researches is in rapid progress now. The presented papers provide a description of recent developments and original results obtained by authors in some specific areas of this very wide scientific field. We hope that the Volume will be of interest for those specialized in the subject of laser-matter interactions.

INTECH
open science | open minds

InTech Europe
University Campus STeP Ri
Slavka Krautzeka 83/A
51000 Rijeka, Croatia
Phone: +385 (51) 770 447
Fax: +385 (51) 686 166
www.intechopen.com

InTech China
Unit 405, Office Block, Hotel Equatorial Shanghai
No.65, Yan An Road (West), Shanghai, 200040, China
中国上海市延安西路65号上海国际贵都大饭店办公楼405单元
Phone: +86-21-62489820
Fax: +86-21-62489821

IntechOpen